JCB Journal of Cell Biology

TOOLS

An advanced toolset to manipulate and monitor subcellular phosphatidylinositol 3,5-bisphosphate

Joshua G. Pemberton[1,2,3], Isobel Barlow-Busch[4], Meredith L. Jenkins[4], Matthew A.H. Parson[4], Farkas Sarnyai[1], Seyma Nur Bektas[1], Yeun Ju Kim[1], John E. Heuser[1], John E. Burke[4,5], and Tamas Balla[1]

Phosphatidylinositol (PI) 3,5-bisphosphate (PI(3,5)P_2) is a minor inositol-containing phospholipid that serves as an important regulator of endolysosomal functions. However, the precise sites of subcellular enrichment and molecular targets of this regulatory lipid are poorly understood. Here, we describe the generation and detailed characterization of a short engineered catalytic fragment of the human PIKfyve enzyme, which potently converts PI 3-phosphate to PI(3,5)P_2. This novel tool allowed for the evaluation of reported PI(3,5)P_2-sensitive biosensors and showed that the recently identified phox homology (PX) domain of the *Dictyostelium discoideum* (*Dd*) protein, SNXA, can be used to monitor the production of PI(3,5)P_2 in live cells. Modification and adaptation of the *Dd*SNXA^{PX}-based probes into compartment-specific bioluminescence resonance energy transfer–based biosensors allows for the real-time monitoring of PI(3,5)P_2 generation within the endocytic compartments of entire cell populations. Collectively, these molecular tools should allow for exciting new studies to better understand the cellular processes controlled by localized PI(3,5)P_2 metabolism.

Introduction

Phosphatidylinositol (PI) 3,5-bisphosphate (PI(3,5)P_2) is a minor polyphosphoinositide (PPIn) lipid generated by the essential and evolutionarily conserved PI 3-phosphate (PI3P) 5-kinase enzyme, PIKfyve (Fab1 in yeast). In eukaryotic cells, the resting levels of PI(3,5)P_2 are extremely low, representing less than ~0.1% of the total inositol-containing phospholipids (Jin et al., 2016). The levels of PI(3,5)P_2 significantly increase after hyperosmotic shock, which was first reported in yeast (Dove et al., 1997), but has since been observed in plants (Meijer et al., 1999) and to a lesser degree in mammalian cells (Jin et al., 2017). PIKfyve generates PI(3,5)P_2 from PI3P, which is found primarily in early and, to a smaller extent, late endolysosomes (e.g., Pemberton et al., 2020) while also serving as an essential component for membranes of nascent autophagosomes (Yu et al., 2018). Accordingly, PI(3,5)P_2 has been implicated as an important regulatory signal for a number of biological processes associated with endolysosomal functions (see Jin et al. [2016]; Rivero-Ríos and Weisman [2022]; Shisheva [2012] for original citations).

PIKfyve is part of a larger macromolecular complex that is formed with the inositol lipid phosphatase, Fig4 (also called Sac3), and the scaffolding protein, Vac14 (also called ArPIKfyve) (Duex et al., 2006; Rudge et al., 2004; Sbrissa et al., 2008). Recent structural studies suggest that the assembled PIKfyve complex is comprised of five copies of Vac14 and one copy each of PIKfyve and Fig4 (Lees et al., 2020). While it was shown that the Fig4 phosphatase is active when assembled in the complex and can essentially reverse the reaction catalyzed by PIKfyve, the regulatory significance of having these opposing enzymatic activities in the same complex is poorly understood. Nevertheless, loss of Fig4 actually decreases, rather than increases, PI(3,5)P_2 levels, with this response being mediated by either instability of PIKfyve in the absence of Fig4, which would thereby reduce PIKfyve levels (Chow et al., 2007), or Fig4 regulating an inhibitory phosphorylation site within PIKfyve (Lees et al., 2020).

Most of our understanding of PIKfyve function is based on studies that used potent PIKfyve inhibitors or genetic inactivation of either the enzyme or its associated proteins. Temperature-sensitive alleles of Fab1 in yeast display marked enlargement of vacuoles at the nonpermissive temperature (Yamamoto et al., 1995), and swollen endolysosomes are also hallmarks of mammalian cells treated with PIKfyve

[1]Section on Molecular Signal Transduction, Eunice Kennedy Shriver National Institute of Child Health and Human Development, National Institutes of Health, Bethesda, MD, USA; [2]Department of Biology, Western University, London, Canada; [3]Division of Development and Genetics, Children's Health Research Institute, London, Canada; [4]Department of Biochemistry and Microbiology, University of Victoria, Victoria, Canada; [5]Department of Biochemistry and Molecular Biology, University of British Columbia, Vancouver, Canada.

Correspondence to Tamas Balla: ballat@mail.nih.gov; John E. Burke: jeburke@uvic.ca.

inhibitors, including YM201636 (Jefferies et al., 2008), apilimod (Cai et al., 2013), or the recently identified WX8 family inhibitors (Sharma et al., 2019) and ESK981 (Qiao et al., 2021). Pathogenic loss-of-function mutations in PIKfyve or its binding partners have also been described (Gee et al., 2015; Lenk et al., 2011; Zhang et al., 2007). PIKfyve is an essential gene in mice (Ikonomov et al., 2011) and in other organisms (Nicot et al., 2006; Rusten et al., 2006), yet PIKfyve has been identified as a potential therapeutic target in a number of human diseases (Burke et al., 2023). Recently, PIKfyve inhibitors showed promise in improving symptoms of ALS in various mouse models (Hung et al., 2023) and have been found effective against cancer cells that depend on increased autophagy, such as melanoma (Qiao et al., 2021; Sharma et al., 2019). Inhibition of PIKfyve was also reported to inhibit infection by selected viruses, including SARS-CoV-2 (Kang et al., 2020), although using it as an antiviral agent in humans may not be feasible (Baranov et al., 2020). Apilimod, the most clinically progressed PIKfyve inhibitor, was initially identified as an inhibitor of Toll-like receptor–induced interleukin-12 (IL-12) and IL-23 cytokine production (Wada et al., 2007), and used in clinical trials for the treatment of several diseases, including B-cell non-Hodgkin lymphoma (Gayle et al., 2017), psoriasis, rheumatoid arthritis, and Crohn's disease (Krausz et al., 2012; Sands et al., 2010; Wada et al., 2012) even before it was known that it selectively inhibits PIKfyve.

Several downstream molecular targets responding to changes in $PI(3,5)P_2$ levels have been proposed, namely, the autophagy-related WIPI (WD-repeat protein interacting with phosphoinositides) protein family (Dove et al., 2009; Liang et al., 2019), WD40 domain–containing protein raptor (Bridges et al., 2012), transient receptor potential mucolipin channel (Dong et al., 2010), ClC-7 chloride–proton antiporter (Leray et al., 2022), V_0 subunit of the V-ATPase proton pump (Banerjee et al., 2019; Li et al., 2014), and some members of the sorting nexin (SNX) family (Sultana et al., 2020; Vines et al., 2023; Xu et al., 2020). Also, numerous processes and steps related to endosomal trafficking have been shown to be regulated by PIKfyve and loss-of-function mutations in the PIKfyve/Vac14/Fig4 complex have been identified in a variety of human diseases (see Rivero-Ríos and Weisman [2022]; Shisheva [2012] for details).

One major obstacle that has limited the progress of the $PI(3,5)P_2$ field has been the lack of molecular tools for monitoring the subcellular localization and kinetics of $PI(3,5)P_2$ levels in live cells and approaches that can spatially induce acute changes in $PI(3,5)P_2$ levels to determine effectors that would respond to such manipulations. An exciting recent study has seemingly solved one of these problems by identifying the phox homology (PX) domain of sorting nexin A (SNXA) from *Dictyostelium discoideum (Dd)*, which we refer to here as *Dd*$SNXA^{PX}$, as a bona fide $PI(3,5)P_2$ reporter (Maib et al., 2024; Vines et al., 2023; Weckerly and Hammond, 2023). In the present study, we introduce and characterize an engineered catalytically active fragment of PIKfyve that allows the rapid production of $PI(3,5)P_2$ upon recruitment from the cytosol to the membranes of selected organelles. Biochemical and biophysical analysis of this PIKfyve fragment identifies conformational changes that accompany membrane binding of the enzyme.

Results

PIKfyve predicted structure and characterization of a truncated PIKfyve construct

To provide insight into the structural regulation PIKfyve, we modeled the assembled complex of PIKfyve with its regulatory proteins Vac14 and Fig4 using AlphaFold3 (Abramson et al., 2024) (Fig. 1 A). The flow path utilized to generate this model, and the validation statistics are shown in Fig. S1. We generated a high-confidence model of pentameric Vac14 bound to a single copy of Fig4 and PIKfyve. The Fig4 bound at the N-terminal end of two Vac14 subunits, with PIKfyve bound to a single Vac14 subunit on the opposite face of the Fig4-Vac14 interface. The overall predicted domain topology of the PIKfyve-Vac14-Fig4 complex corresponds broadly to the model determined through medium- to low-resolution cryo-EM density data (Lees et al., 2020). The predicted structure of PIKfyve showed that the PI3P-binding FYVE (128–223) (Sbrissa et al., 2002) and DEP (349–440) domains were flexible relative to the other PIKfyve domains (i.e., these domains are folded but have weak predicted alignment error to the rest of the PIKfyve ordered domains). There were also a number of disordered loops in PIKfyve with no apparent secondary structure. These domains/loops were omitted from the model shown in Fig. 1 A. There was no direct interface between the kinase domain and Vac14, with the CCT/CCR domains (585–884, 1032–1382) acting as an interface for both Vac14 and the PIKfyve kinase domain. The N-terminal region of the CCT/CCR packs against Vac14, as previously experimentally determined by cryo-EM (Lees et al., 2020), with the C-terminal region of the CCT/CCR packing against the PIKfyve kinase domain. Intriguingly, our modeling revealed an interfacial loop (residues 1127–1162) at the end of a long disordered loop in the CCT/CCR region that packs against both Fig4 and Vac14 at the opposite side of Vac14 compared with the main CCT/CCR interface. This may provide some molecular insight into why PIKfyve only interacts with Vac14 when Fig4 is present, and also why it selectively binds to Vac14 on the opposite face of the Fig4-Vac14 interface. Further biophysical and biochemical validation will be required to define the importance of this region in the PIKfyve-Vac14-Fig4 complex assembly.

Our model of PIKfyve showed that the CCT/CCR domains are connected by a short linker region (1383–1405) to a three-helix bundle (3HB, 1405–1522) that together both pack against the kinase domain. The linker makes extensive contacts with the C-lobe of the kinase domain (Fig. 1 B). Intriguingly, the linker between the CCT/CCR and 3HB crosses the catalytic cleft of the kinase domain and mimics the conformation of the insert region following helix α7 in the related PPIn kinase families, PI5P4Ks and PI4P5Ks (Fig. 1 C). Using the AlphaFold3 predicted structure, we generated an optimized PIKfyve core construct that consists of residues 1383–1522, 1629–1706, and 1796–2098 joined by short glycine-rich linkers (Fig. 1 D). The FYVE, DEP, and CCT/CCR domains were removed, as well as

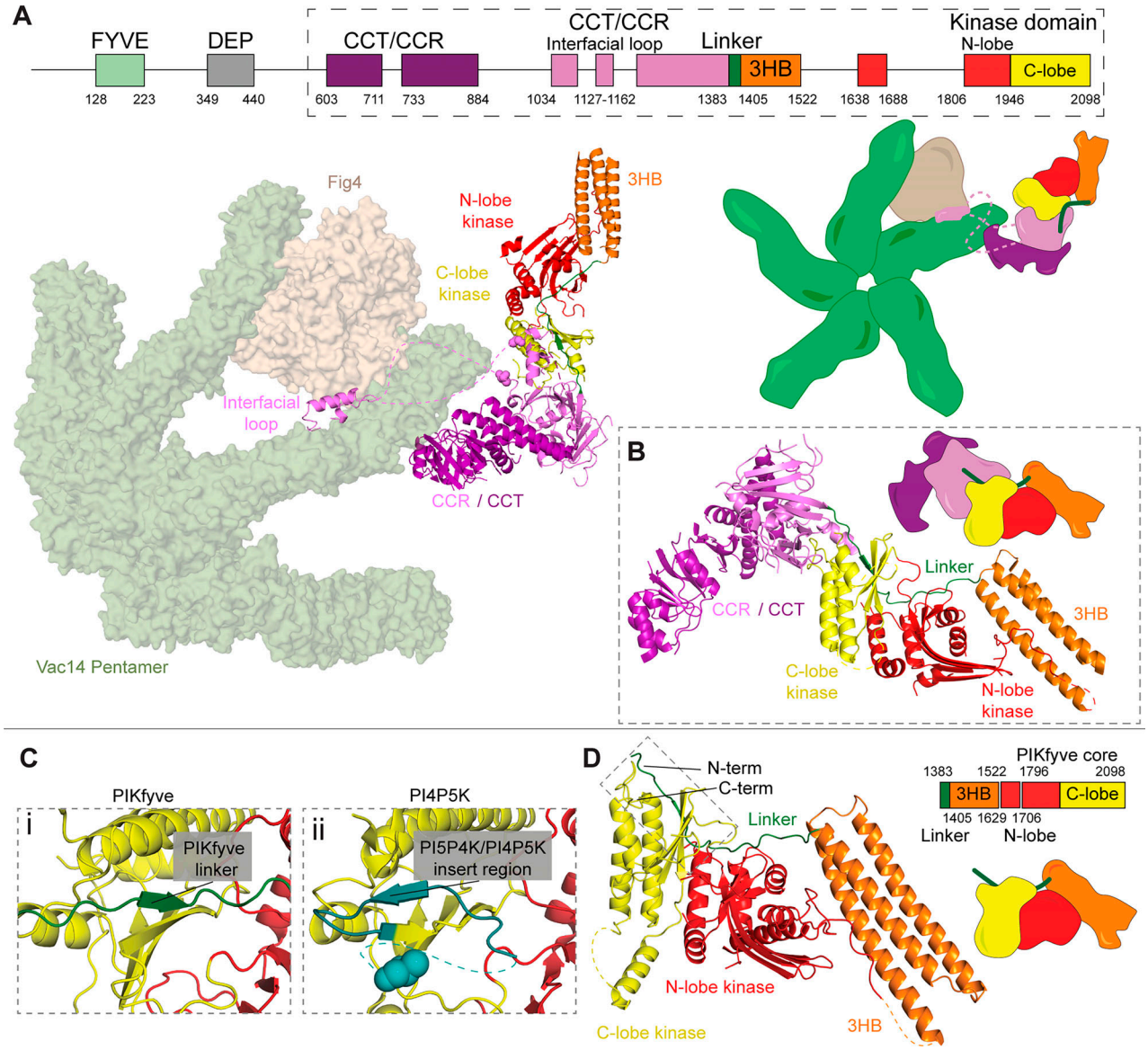

Figure 1. **Predicted modeling of the PIKfyve complex, generation of a catalytic core construct of PIKfyve, and comparison with PPIn kinases. (A)** Domain schematic of full-length *H. sapiens* PIKfyve and AlphaFold3 predicted structure of PIKfyve, Fig4, and the Vac14 pentamer with low-confidence regions (pLDDT <50) removed (Abramson et al., 2024) (see Fig. S1 for full modeling details). The ordered FYVE and DEP domains are omitted from the full-length PIKfyve structure because they are likely dynamic relative to the rest of the protein (see the PAE plot in Fig. S1). **(B)** AlphaFold3 predicted structure of the boxed region of PIKfyve from the schematic in A. **(C)** Comparison of the insert region in PI4P5Kα (PDB:4TZ7) with the linker between the CCR/CCT and 3HB domains of PIKfyve. **(D)** Domain schematic and AlphaFold3 predicted structure for the PIKfyve^{CC} with low-confidence regions (pLDDT <50) removed. Domains are colored to match the domain schematics in A. PAE, predicted aligned error.

the disordered regions between the 3HB and the kinase domain. We expressed the truncated PIKfyve (which will be referred to as PIKfyve catalytic core [^{CC}], or PIKfyve^{CC}) construct in Sf9 cells, with it expressing in greatly increased yield compared with full-length PIKfyve. The PIKfyve^{CC} eluted from gel filtration at a volume consistent with it being strictly monomeric (~60 kDa) (Fig. 2 A). This contrasts from the formation of homodimers in the evolutionarily related PI4P5Ks and PI5P4Ks (Hu et al., 2015; Rao et al., 1998), with predicted steric contacts present in PIKfyve that would prevent dimerization through either the PI5P4K or PI4P5K dimer interfaces (Fig. 2 B).

To confirm the ordered nature of this construct, we used hydrogen–deuterium exchange mass spectrometry (HDX-MS) to identify regions of order and disorder within the PIKfyve^{CC}. HDX-MS measures the deuterium incorporation of amide hydrogens, with the exchange rate of hydrogen to deuterium therefore dependent on the secondary structure, making it a powerful tool to investigate protein dynamics (Masson et al., 2017, 2019). Deuterium incorporation is observed at peptide-level resolution through the generation of pepsin-digested peptides following exposure to deuterated solvent. We carried out a pulse HDX experiment, where the PIKfyve core was exposed to deuterium for 3 s, with regions containing secondary

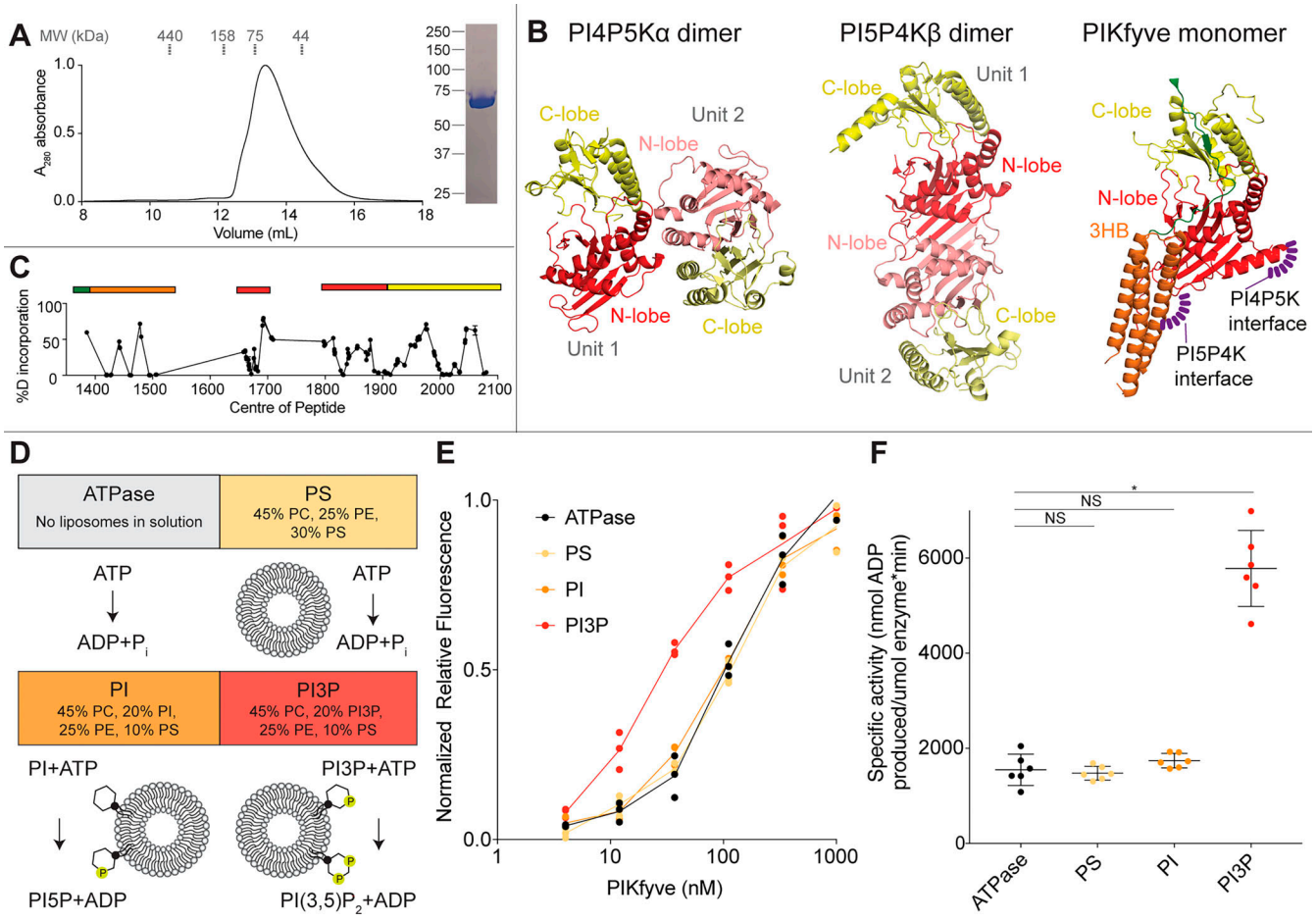

Figure 2. **Biochemical analysis of a catalytic core construct of PIKfyve, and comparison with PPIn kinases. (A)** Gel filtration elution profile of the PIKfyve^{CC}, with size standards indicated. The SDS-PAGE of this fraction is shown to the right. **(B)** Structures of the type I PI4P5Kα and type II PI5P4Kβ dimers (PDB: 4TZ7, 3X03) (Hu et al., 2015; Sumita et al., 2016) compared with the monomeric PIKfyve^{CC}. Steric clashes, as indicated, prevent dimerization seen in type I and type II PIP kinases. **(C)** Relative percentage of deuterium incorporation after 3 s of D_2O exposure at 19°C. Each point represents a single peptide graphed in the x axis according to its central residue, with the domain architecture of the PIKfyve^{CC} above. **(D)** Schematic of liposomes generated for PIKfyve^{CC} activity assays. ATPase conditions contained ATP but no liposomes in solution; PS liposomes contained 45% PC, 25% PE, and 30% PS; PI liposomes contained 45% PC, 20% PI, 25% PE, and 10% PS; and PI3P liposomes contained 45% PC, 20% PI3P, 25% PE, and 10% PS. **(E)** Measurement of ATP turnover performed with different liposomes in solution with the PIKfyve^{CC} (see D for liposome conditions). Experiments were performed with 1,000–4.11 nM PIKfyve^{CC} with a final concentration of 0.2 mg/ml of liposomes and 100 µM ATP. **(F)** Specific activity values for the ATPase assays performed with different liposomes in solution with the PIKfyve^{CC} (technical replicates; data are presented as mean values, and error bars are SD, n = 3). Specific activity was calculated using the concentrations where kinase activity was in range (111 and 37 nM for ATPase, PI, and PS, and 37 and 12 nM for PI3P). Two-tailed t test P values represented by the symbols are as follows: * < 0.0001.

structure being protected, and unstructured regions being exchanged. The HDX results were consistent with the AlphaFold3 predicted structure (Fig. 2 C).

To validate that the PIKfyve^{CC} was catalytically active, we carried out biochemical assays of ATP turnover. We used multiple substrates, including ATP alone or ATP in combination with the following liposomes: liposomes lacking any PI or PPIn substrate (45% PC, 25% PE, and 30% PS, called PS liposomes), liposomes where PS was replaced by 20% PI substrate (called PI liposomes), and liposomes containing 20% PI3P substrate (called PI3P liposomes) (Fig. 2 D). There was no significant difference in activation between PI and PS liposomes compared with basal ATPase activity, with only increased ATP turnover present with PI3P liposomes (approximately threefold increase in ATP turnover) (Fig. 2, E and F). This suggests that under these conditions, the PIKfyve^{CC} has very limited ability to convert PI to PI 5-phosphate at above basal ATPase levels, but can generate PI(3,5)P_2 from PI3P, which is consistent with prior cellular analysis of PIKfyve substrate selectivity (Zolov et al., 2012).

HDX-MS reveals conformational changes in the PIKfyve^{CC} during association with substrate membranes

Having established that the PIKfyve^{CC} has activity on PI3P liposomes, we carried out HDX-MS experiments to define conformational changes that occur upon membrane binding. HDX-MS is a powerful tool to analyze conformational changes that occur upon peripheral proteins binding to membrane surfaces, which have been challenging to study by other structural techniques (Vadas et al., 2017). Deuterium incorporation was

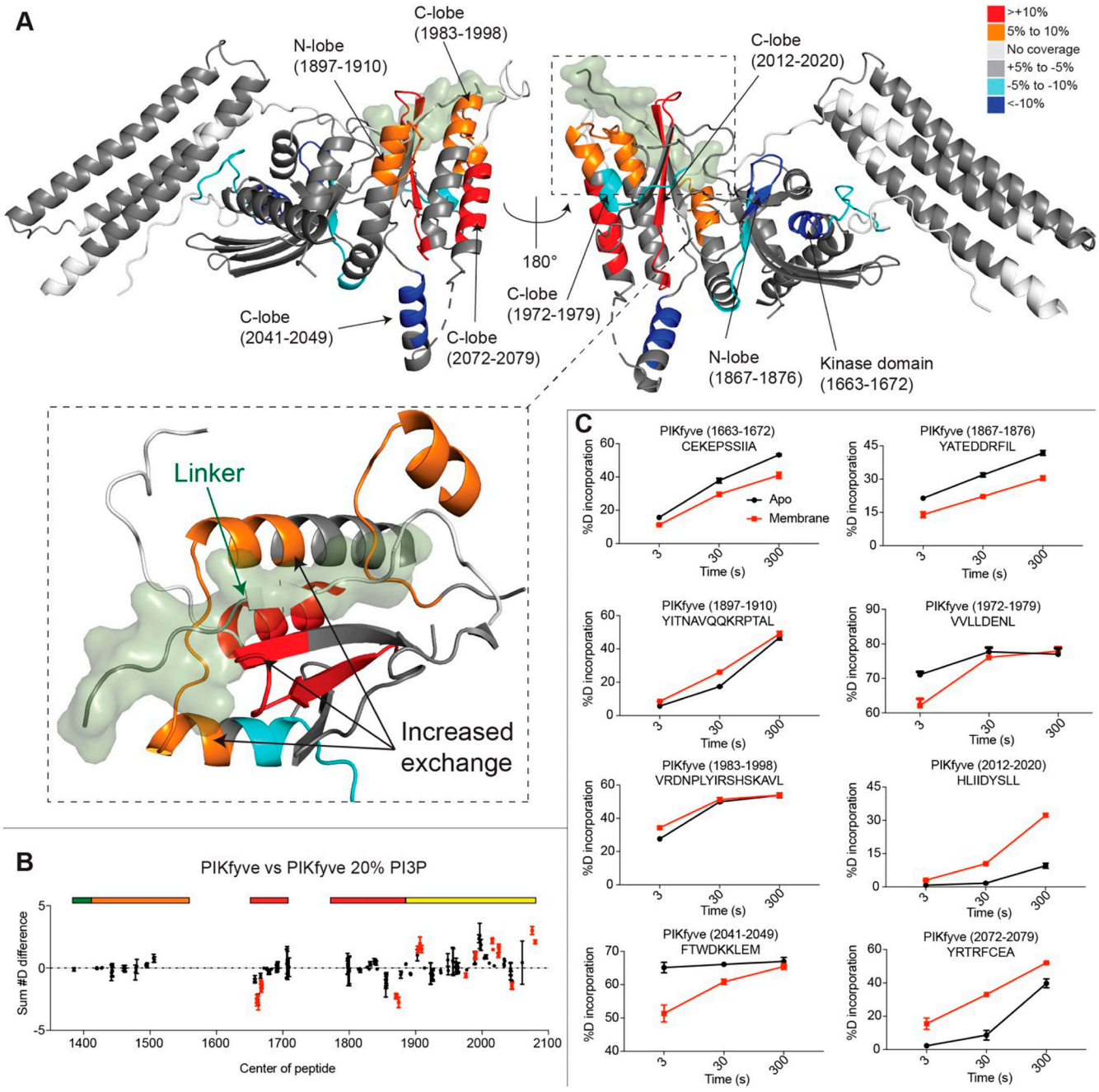

Figure 3. **HDX-MS differences upon PIKfyve^{CC} binding to PI3P liposomes. (A)** Peptides in the PIKfyve^{CC} showing significant differences in deuterium exchange (defined as >0.45 Da, >5% difference, and P < 0.01 in a two-tailed *t* test) upon binding to 20% PI3P/45% PC/25% PE/10% PS liposomes. Differences are mapped on the predicted structure for the PIKfyve^{CC} from Fig. 1 B, with an expanded view of the linker region shown below, with the linker shown as a green surface. **(B)** Sum of the number of deuteron differences for all peptides analyzed over the entire time course for the PIKfyve^{CC} upon binding PI3P liposomes. Peptides colored in red are those that had a significant change (defined as >0.45 Da, >5% difference, and P < 0.01 in a two-tailed *t* test). Each time point represents a single peptide, and error bars are shown as the sum of SD across all time points (n = 3 for each time point except: n = 2 for 30s membrane binding, 300s membrane 1980–2013, 300s membrane 1983–2008, 30s apo 1941–1956, 300s apo 1983–2008). The domain architecture of the PIKfyve^{CC} is noted above the primary sequence. The full HDX data are available in the source data. **(C)** Selected PIKfyve^{CC} peptides that showed significant increases or decreases in exchange upon binding PI3P liposomes. Mean is shown, with error bars representing SD (n = 3).

measured over three time points of exchange (3, 30, and 300 s at 18°C), and the HDX-MS coverage map of the PIKfyve^{CC} was composed of 123 peptides that spanned 89.8% of the primary sequence for the PIKfyve^{CC} construct (Table S1). Significant differences in exchange were defined as differences in any time point fitting the following three criteria: >5%, >0.45 Da, and a two-tailed *t* test P < 0.01.

We observed both increased and decreased exchange in many areas of the PIKfyve^{CC} upon membrane binding, particularly within the kinase domain (Fig. 3, A–C and Fig. 2 C). Several

peptides in the kinase domain showed decreased deuterium incorporation upon membrane binding, including those corresponding to residues 1652–1671 and 1866–1881 of the N-lobe, and 1972–1979 of the C-lobe (Fig. 3, B and C), as well as the activation loop (2041–2049) in the C-lobe. These regions are in the predicted membrane binding regions. Intriguingly, there were multiple regions that unexpectedly showed increased exchange on membrane binding. Regions with the largest increases in exchange in the PIKfyve^{CC} include 1897–1910, 1983–1998, 2012–2020, and 2072–2079 of the kinase domain, which interact directly with the predicted beta strand present in the linker region (Fig. 3, B and C). This exposure surrounding the linker region upon membrane binding suggests that a conformational change is induced in which the linker region releases and primes the protein for catalytic activity. These results are both consistent with the AlphaFold3 model and reveal insight into conformational dynamics of PIKfyve upon membrane binding. Intriguingly, these results suggest that a critical feature of PIKfyve activation might involve disruption of the interface between the CCT/CCR domains and kinase domain, as has been previously suggested in yeast (Lang et al., 2017), with this rearrangement involving disengagement of the linker region.

The isolated PIKfyve^{CC} is highly active when expressed in mammalian cells

Next, we wanted to determine whether the PIKfyve^{CC} fragment could be used to manipulate the levels of PI(3,5)P_2 in live cells. For this, we fused the PIKfyve^{CC} to an FKBP recruitment module that allows for the chemically inducible translocation of the engineered PPIn kinase from the cytosol to specific subcellular membranes tagged with FRB. This recruitment system relies on the rapamycin-induced heterodimerization between FKBP12 and the small FRB fragment of mTOR (Choi et al., 1996), which have been widely used to chemically induce the rapid rerouting of molecules to defined organelle membranes (Suh et al., 2006; Varnai et al., 2006). First, we tested whether the expression of the FKBP-PIKfyve^{CC} affects the steady-state levels of PI3P using established reporters, which are based on either the FYVE domain of EEA1 (Várnai and Balla, 2006) or the high-affinity tandem (2x)FYVE from Hrs (Gillooly et al., 2000). Active PIKfyve is expected to convert PI3P to PI(3,5)P_2, thereby effectively decreasing the levels of the PI3P substrate. Indeed, HEK293A cells expressing the FKBP-PIKfyve^{CC}, together with a Rab5-targeted FRB (iRFP-FRB-Rab5) (Baba et al., 2019), showed a greatly reduced signal of the endosomal PI3P sensor (EGFP-(2x)FYVE^{Hrs}), particularly in cells that expressed high levels of the FKBP-PIKfyve^{CC} fragment (Fig. 4 A). However, after the addition of the PIKfyve inhibitor, apilimod (1 µM), the PI3P signal associated with endosomes gradually increased (Fig. 4 A and Video 1), suggesting that the expressed FKBP-PIKfyve^{CC} is already active from the cytoplasm. Rapamycin induced recruitment of the enzyme to Rab5-positive compartments in cells with low levels of FKBP-PIKfyve^{CC} expression, and hence still showing the endosomal PI3P signal, which in this case was monitored by the lower affinity EGFP-FYVE^{EEA1}, the recruited enzyme rapidly eliminated the PI3P signal from the endosomes (Fig. 4 B and Video 2). Importantly, this induced clearance of PI3P by FKBP-PIKfyve^{CC} recruitment was rapidly reversed by apilimod. These studies reveal that the low-level expression of the FKBP-PIKfyve^{CC} can be combined with endosomal-specific enzyme recruitment to locally consume membrane PI3P.

Direct monitoring of localized PI(3,5)P_2 production following FKBP-PIKfyve^{CC} recruitment

Having established that the PIKfyve^{CC} is active, we set out to determine whether PI(3,5)P_2 formation could be detected directly using previously reported PI(3,5)P_2-selective biosensors. For this, we first turned to the recently identified PI(3,5)P_2-binding probe, *Dd*SNXA^{PX} (Vines et al., 2023), and generated PX domain (Residues 61–175) variants containing flexible interdomain linkers that were based on the reported homodimeric orientation of the full-length SNXA. The expression of a monomeric *Dd*SNXA^{PX}-based reporter as a mNeonGreen (human codon–optimized [^{HO}])-fused protein (mNG^{HO}-*Dd*SNXA^{PX}) in HEK293A cells showed no recognizable subcellular enrichment regardless of the relative expression level. The only slight enrichment we observed was to the nucleolus (Fig. S2 A). When a tandem (2x) version was used (mNG^{HO}-(2x)*Dd*SNXA^{PX}), the nuclear localization was more prominent, with some nuclear speckles in addition to the slight nucleolar enrichment (Fig. S2 B). The only extranuclear localization was a punctate structure in the centrosomal area, which was observed in only some cells, and none of this localization was changed after the addition of apilimod (1 µM; Fig. S2 B). Considering the extremely low resting levels of PI(3,5)P_2, the lack of localization to any subcellular structures was not unexpected, especially since any minor membrane residency would be unrecognizable against the high relative cytoplasmic signal that was even associated with extremely low expression levels. Moreover, given its insensitivity to apilimod treatment, the nuclear and centrosome localization was also considered to be unrelated to PI(3,5)P_2. Next, we expressed these sensors together with the recruitable FKBP-PIKfyve^{CC} enzyme and a Rab5-targeted FRB recruiter construct. The single *Dd*SNXA^{PX} sensor still showed no prominent localization before recruitment. However, when the active FKBP-PIKfyve^{CC} enzyme was recruited to Rab5-positive compartments, the mNG^{HO}-*Dd*SNXA^{PX} construct showed a clear translocation to membranes decorated with the FKBP-PIKfyve^{CC} (Fig. 5 A). Importantly, the membrane binding of the *Dd*SNXA^{PX} probe was rapidly reversed after the addition of apilimod (1 µM; Fig. 5 A). In several cells, the tandem mNG^{HO}-(2x)*Dd*SNXA^{PX} reporter already showed punctate localization in the cytosol of cells expressing the active FKBP-PIKfyve^{CC}, even without recruitment to any membrane compartment (Fig. S2 C). To minimize the nuclear signal and increase the cytosolic fraction of the probe, we added tandem nuclear export signals (NES$^{(2x)}$) within the mNG^{HO} backbone (NES$^{(2x)}$-mNG^{HO}-(2x)*Dd*SNXA^{PX}). The localization of this reporter to the Rab5 compartment was significantly enhanced by locally recruiting the FKBP-PIKfyve^{CC}, and the observed enrichment of the reporter was then completely reversed after apilimod treatment (1 µM; Fig. 5 B and Video 3). To show that this PI(3,5)P_2 increase, indeed, reflected the conversion of PI3P by the enzyme in the same Rab5 compartment, we simultaneously monitored the PI3P

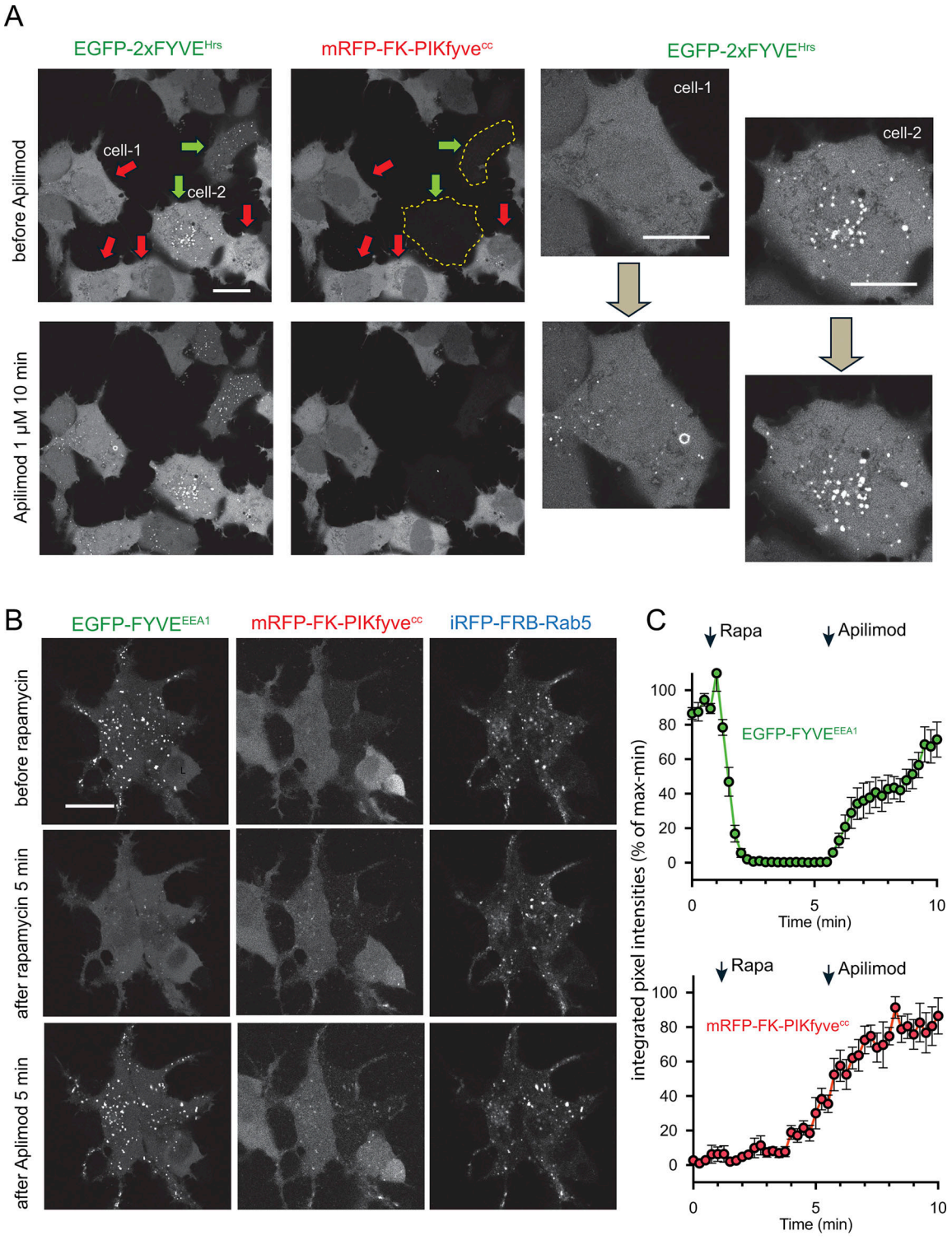

Figure 4. **Effect of PIKfyve^{CC} expression on subcellular PI3P levels. (A and B)** Confocal images of HEK293A cells transfected with the PI3P sensor, EGFP-(2x)FYVE^{Hrs} (A) or EGFP-FYVE^{EEA1} (B), together with the recruitable mRFP-FKBP-PIKfyve^{CC} fragment. Note that cells expressing the PIKfyve^{CC} fragment show no PI3P-positive structures (red arrows), while those with no detectable enzyme (green arrows and outlined with dotted yellow lines) show the characteristic subcellular PI3P signal. Apilimod treatment (1 µM, 10 min) causes the reappearance of the PI3P-positive structures, suggesting that the disappearance of PI3P is due to the presence of the catalytically active PIKfyve^{CC} fragment. Enlarged images of cell-1 and cell-2 before and after apilimod are also shown on the right. **(B)** HEK293A cells were transfected with the PI3P sensor, EGFP-FYVE^{EEA1}, together with the recruitable mRFP-FKBP-PIKfyve^{CC} enzyme and a Rab5-targeted FRB fragment (iRFP-FRB-Rab5). Cells that express all three constructs and still show PI3P signal associated with their endosomes were subjected to rapamycin treatment (100 nM, 5 min), which results in rapid loss of the membrane-bound PI3P signal from the endosomes as the FKBP-PIKfyve^{CC} fragment is recruited to the Rab5 compartment. Apilimod treatment (1 µM, 5 min) reverses the effect of the recruited enzyme. **(C)** Quantification of these changes from five individual cells is shown from one representative recording (mean ± SEM). Note that PI3P (green) rapidly disappears even when the amount of recruited enzyme (red) is barely detectable (scale bars = 10 µm).

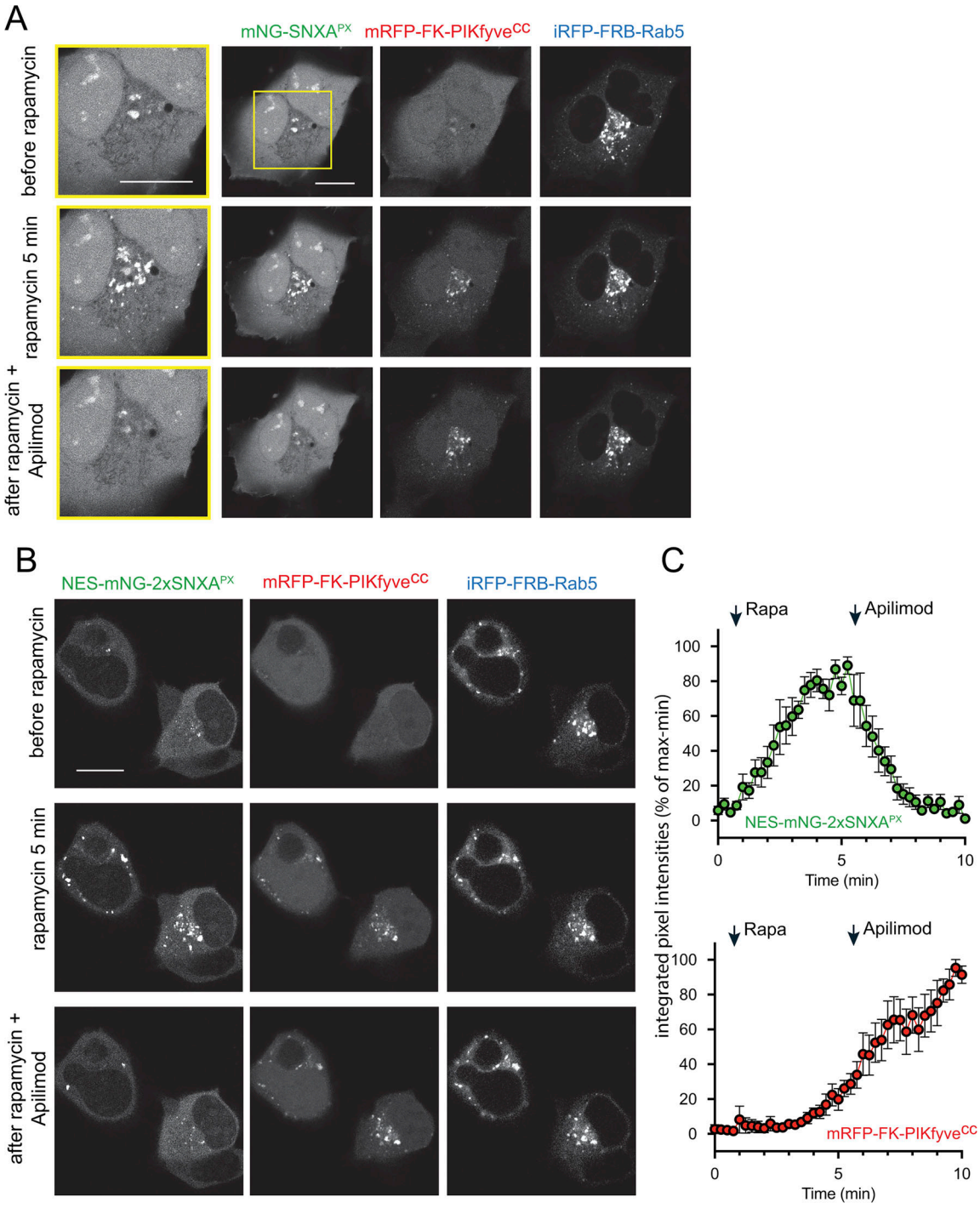

Figure 5. **Effect of PIKfyve^{CC} expression on cellular PI(3,5)P_2 levels as monitored by the PX domain of *D. discoideum* (*Dd*) SNXA. (A)** Confocal images of HEK293A cells transfected with the PI(3,5)P_2 sensor, mNG^{HO}-*Dd*SNXA^{PX}, together with the recruitable mRFP-FKBP-PIKfyve^{CC} enzyme and Rab5-targeted FRB fragment (iRFP-FRB-Rab5). Expression of the mNG^{HO}-*Dd*SNXA^{PX} shows enrichment associated with the nucleus and nucleolus, as well as in the centrosomal area, but no endosomal localization. The addition of rapamycin (100 nM, 5 min) causes rapid association of the enzyme with the Rab5-positive endosomes and a corresponding increase in the local mNG^{HO}-*Dd*SNXA^{PX} signal. Endosomal association of the mNG^{HO}-*Dd*SNXA^{PX} signal is reversed by treatment with apilimod (1 µM, within 10 min), but the nuclear- and centrosome-associated signals remain. The left panels show higher magnification images of the boxed inset. **(B)** Experiment performed as in A but using the NES$^{(2x)}$-mNG^{HO}-(2x)SNXA^{PX} construct as the PI(3,5)P_2 reporter. **(C)** Quantification of the changes from six cells obtained in one representative time-lapse recording (mean ± SEM). Note that PI(3,5)P_2 (green) already appears even when the amount of recruited enzyme (red) is barely detectable (scale bars = 10 µm).

(mCherry-FYVE^{EEA1}) and PI(3,5)P_2 (NES-mNG^{HO}-(2x)*Dd*SNXA^{PX}) biosensors during recruitment of the PIKfyve^{CC} fragment to Rab5 endosomes. Such experiments showed the reciprocal changes between PI3P and PI(3,5)P_2 in the same compartment (Fig. S3 and Video 4).

These findings together suggested that resting PI(3,5)P_2 levels are extremely low in most cells, such that even a specific PI(3,5)P_2-recognizing domain is unable to detect enrichment of this lipid against the cytoplasmic signal associated with the expression of the reporter. Serendipitously, when using a line of HEK293 cells expressing the AT1 angiotensin receptor (HEK293-AT1), which was previously generated and widely used by our group (Hunyady et al., 2002), we did observe the high-avidity (NES$^{(2x)}$-mNG^{HO}-(2x)*Dd*SNXA^{PX}) probe associated with a few endosomal structures, even without the overexpression of the PIKfyve^{CC} fragment (Fig. 6). To identify these compartments, we co-expressed the NES$^{(2x)}$-mNG^{HO}-(2x)*Dd*SNXA^{PX} probe with various endosomal markers or in cells incubated with LysoTracker Red. In almost all cases, the PI(3,5)P_2-positive endosomes also contained very bright speckles attached to their periphery. None of these structures were co-localized with Rab5-positive endosomes (Fig. 6 A and Fig. S4). In contrast, they did show co-localization with a fraction of Rab7-positive endosomes (Fig. 6 B and Fig. S4). Importantly, the PI(3,5)P_2-positive structures only overlapped with a fraction of the LAMP1-positive endosomes, which clearly did not show co-localization with the bright speckles (Fig. 6 C and Fig. S4). Curiously, the PI(3,5)P_2-positive structures mostly did not co-localize with the small bright LysoTracker signal (Fig. 6 D). However, some PI(3,5)P_2-positive signal did touch the LysoTracker-positive lysosomes, and in some cases, they were detectable within enlarged lysosomes/multivesicular bodies (Fig. 6 D). Apilimod treatment (1 μM) eliminated the labeling of these structures with the (2x)*Dd*SNXA^{PX} reporter (Fig. 7 A), and similarly, IN-1 (300 nM), an inhibitor of Vps34, the PI 3-kinase that generates the endosomal pool of PI3P, also rapidly reduced the signal (Fig. 7 B). These studies suggest that resting PI(3,5)P_2 levels may differ among various cell lines, including even within the same lineage.

However, irrespective of the resting levels, our ability to acutely produce PI(3,5)P_2 by the FKBP-PIKfyve^{CC} enzyme allows, for the first time, a method to reliably test the specificity and sensitivity of any putative PI(3,5)P_2-recognizing molecular probes. In particular, based on the stringent criteria established for the practical assessment of lipid biosensors (Wills et al., 2018), we can confirm that ectopic PI(3,5)P_2 synthesis is indeed sufficient to drive the membrane enrichment of the newly described *Dd*SNXA^{PX}-based probes.

Measuring the kinetics of inducible FKBP-PIKfyve^{CC} activity at the population scale

Previously, to follow the membrane-selective enrichment of PI3P at the population scale, we created bioluminescence resonance energy transfer (BRET)–based biosensors that contained Rab5-targeted mVenus (mVenus-Rab5) to serve as a membrane-anchored BRET acceptor and then made a lipid-specific BRET donor consisting of super luciferase (sLuc) fused to the (2x)

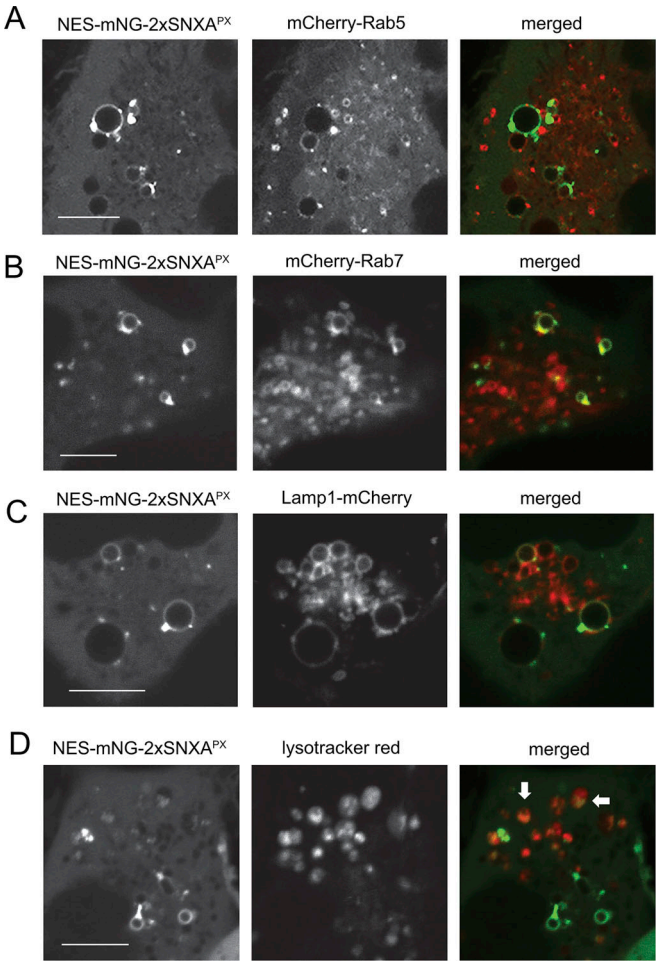

Figure 6. **Detection of PI(3,5)P_2 using the NES$^{(2x)}$-mNG^{HO}-(2x)*Dd*SNXA^{PX} construct in HEK293-AT1 cells. (A–D)** Confocal images of HEK293-AT1 cells transfected with the high-avidity PI(3,5)P_2 probe, NES-mNG^{HO}-(2x)*Dd*SNXA^{PX}, and mCherry-tagged Rab5 (A), mCherry-Rab7 (B), and LAMP1-mCherry (C), or co-stained with LysoTracker Red (D). Importantly, in these cells, PI(3,5)P_2-positive endosomes were apparent even without expressing the PIKfyve^{CC} fragment. Note that the brightest PI(3,5)P_2 signal is not associated with Rab5-positive endosomes and shows the closest co-localization with only a fraction of the Rab7 endosomes. While the PI(3,5)P_2 signal is also associated with a fraction of LAMP1-positive endosomes, the bright "speckles" emanating from the endosome proper only show overlap with Rab7 but not LAMP1. Also, note that the majority of the PI(3,5)P_2 signal does not co-localize with the signal from the LysoTracker Red; however, in some cells the green signal can be seen within the enlarged lysosomes (white arrows). For quantification of images similar to those shown in A–C, see Fig. S4 (scale bars = 5 μm).

FYVE^{Hrs} or FYVE^{EEA1} domains. Both donor and acceptor fusion proteins were expressed in cells from a single plasmid in which the two peptides are separated by a viral 2A peptide sequence (Liu et al., 2017) (Fig. 8 A) (for details of the design, see Pemberton et al. [2020]). The efficiency of the energy transfer between the mVenus and sLuc ultimately depends on relative enrichment of the PI3P-binding (2x)FYVE^{Hrs} sensor specifically within Rab5-positive compartments. Please note that the BRET sensor designed using the FYVE^{EEA1} showed the same relative trends as with the (2x)FYVE^{Hrs}, albeit with a much smaller dynamic range. Using the more sensitive (2x)FYVE^{Hrs}-based BRET

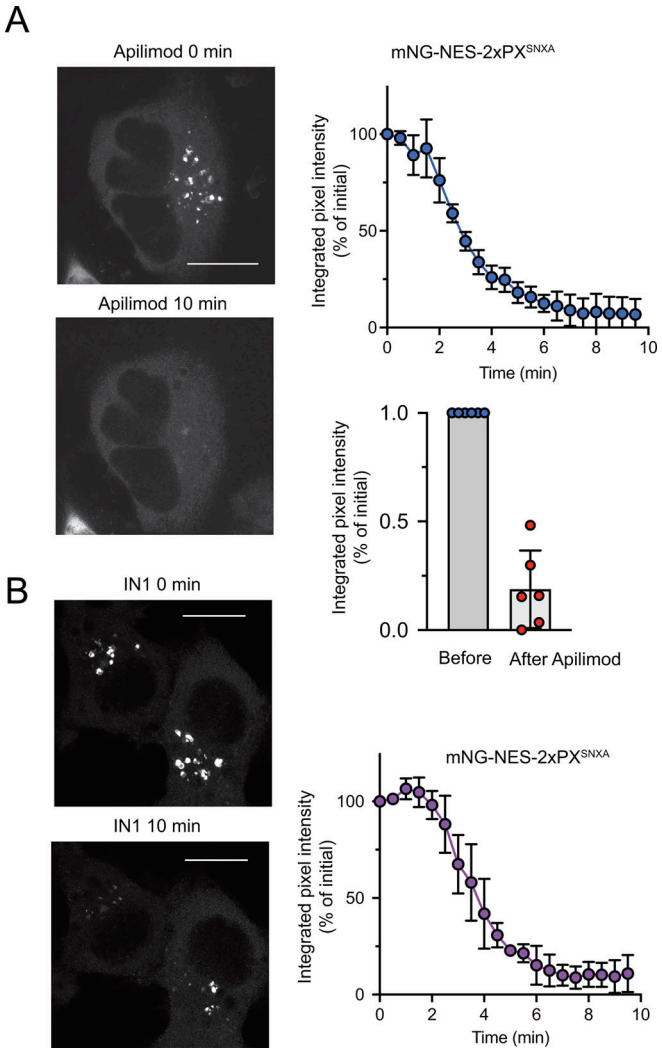

Figure 7. **Inhibition of the PI(3,5)P_2 signal by apilimod or a selective Vps34 inhibitor (IN-1), based on the NES$^{(2x)}$-mNG^{HO}-(2x)*Dd*SNXA^{PX} construct expressed in HEK293-AT1. (A and B)** Confocal images of HEK293-AT1 cells transfected with the high-avidity PI(3,5)P_2 probe, NES$^{(2x)}$-mNG^{HO}-(2x)*Dd*SNXA^{PX}, and treated with either apilimod (1 µM; A) or IN-1 (300 nM; B). Integrated pixel intensities were calculated from orthogonal projections of z-stacks and normalized to the initial value as detailed under Materials and methods for three (A) and two (B) cells obtained in representative time-lapse recordings (mean ± SD). The bar diagram shows integrated pixel intensity values calculated for six cells before and after apilimod treatment recorded in two separate experiments (scale bars = 10 µm).

sensor in combination with endosomal recruitment of the FKBP-PIKfyve^{CC} using FRB-Rab5, results clearly showed the reduced PI3P levels in the Rab5-positive compartment and its rapid further depletion in response to treatment with rapamycin (Fig. 8 B). The addition of apilimod (1 µM) not only reversed the action of the recruited enzyme, but also restored the PI3P levels of the Rab5-positive compartments above the original baseline, which was already reduced by the background catalytic activity even before recruitment of the enzyme fragment (Fig. 8 B). The expression of an inactive (K1877A) (Lang et al., 2017) version of the recruitable FKBP-PIKfyve^{CC} enzyme failed to decrease the basal PI3P levels and did not induce any change to the (2x)FYVE^{Hrs} enrichment after recruitment to the Rab5 compartment (Fig. 8 B).

Next, we created novel BRET constructs to monitor PI(3,5)P_2 production in Rab5-positive endosomes using either the single (NES$^{(2x)}$-sLuc-*Dd*SNXA^{PX}-tPT2A-mVenus-Rab5) or tandem (NES$^{(2x)}$-sLuc-(2x)*Dd*SNXA^{PX}-tPT2A-mVenus-Rab5) *Dd*SNXA^{PX} modules. When designing these BRET biosensors, please note that we used a tandem NES added to the sLuc to maximize the cytosolic fraction of the lipid-binding domains. Using these sensors, we could monitor the production of PI(3,5)P_2 upon recruitment of the FKBP-PIKfyve^{CC} to the Rab5 compartment in entire populations of live cells. In these assays, the resulting signal and dynamic range were much larger when using the tandem (2x)*Dd*SNXA^{PX}-based sensor compared with the single domain (Fig. 8 C). Therefore, we used the tandem version in subsequent experiments. Recruitment of the catalytically active FKBP-PIKfyve^{CC}, but not the inactive K1877A mutant, elicited a large increase in PI(3,5)P_2 levels that was rapidly reversed by apilimod treatment (1 µM; Fig. 8 D). Likewise, pretreatment of the cells with apilimod (1 µM) prevented the generation of PI(3,5)P_2 after rapamycin-induced recruitment of the FKBP-PIKfyve^{CC} domain (Fig. 8 E).

PIKfyve^{CC} does not interact with Vac14 or Fig4

It was important for the proper interpretation of these data to determine whether the isolated PIKfyve^{CC} fragment was able to interact with the endogenous PIKfyve enzyme or its established binding partners. It would be expected that the PIKfyve^{CC} fragment would be unable to bind to Vac14 as it lacks the regions of the enzyme that have been previously established as being required for complex formation (Lees et al., 2020), with our AlphaFold3 modeling further supporting the requirement of the CCT/CCR domains for this interaction (Fig. 1 A). Still, we examined PIKfyve complex formation in live cells using a chemically induced rerouting approach that allows for investigations of protein–protein interactions using folded domains in real time (Robinson et al., 2010). First, we generated a recruitable version of the full-length (FL) human PIKfyve (iRFP-FKBP-PIKfyve^{FL}) and expressed it together with an N-terminally tagged Vac14 (mCherry-Vac14), a C-terminally tagged Fig4 (Fig4-mNG), and an outer mitochondrial membrane (OMM)–targeted FRB tagged with ECFP. Rapamycin treatment recruited the PIKfyve^{FL} to the OMM, which also resulted in parallel translocation of both Vac14 and Fig4, thereby confirming the known interaction between these three proteins (Fig. 9 A and Video 5). We then performed similar experiments using the recruitable FKBP-PIKfyve^{CC} fragment instead of the FKBP-PIKfyve^{FL}. In this case, however, rapamycin addition only caused OMM association of the FKBP-PIKfyve^{CC} fragment, without co-recruitment of Vac14 (Fig. 9 B and Video 6). This experiment was consistent with the model proposed from the cryo-EM structure (Lees et al., 2020), which supports that the catalytic fragment of the PIKfyve^{CC} would not associate with Vac14 and therefore cannot nucleate ectopic assembly of the established PIKfyve macromolecular complex when used to locally manipulate membrane PI(3,5)P_2 levels.

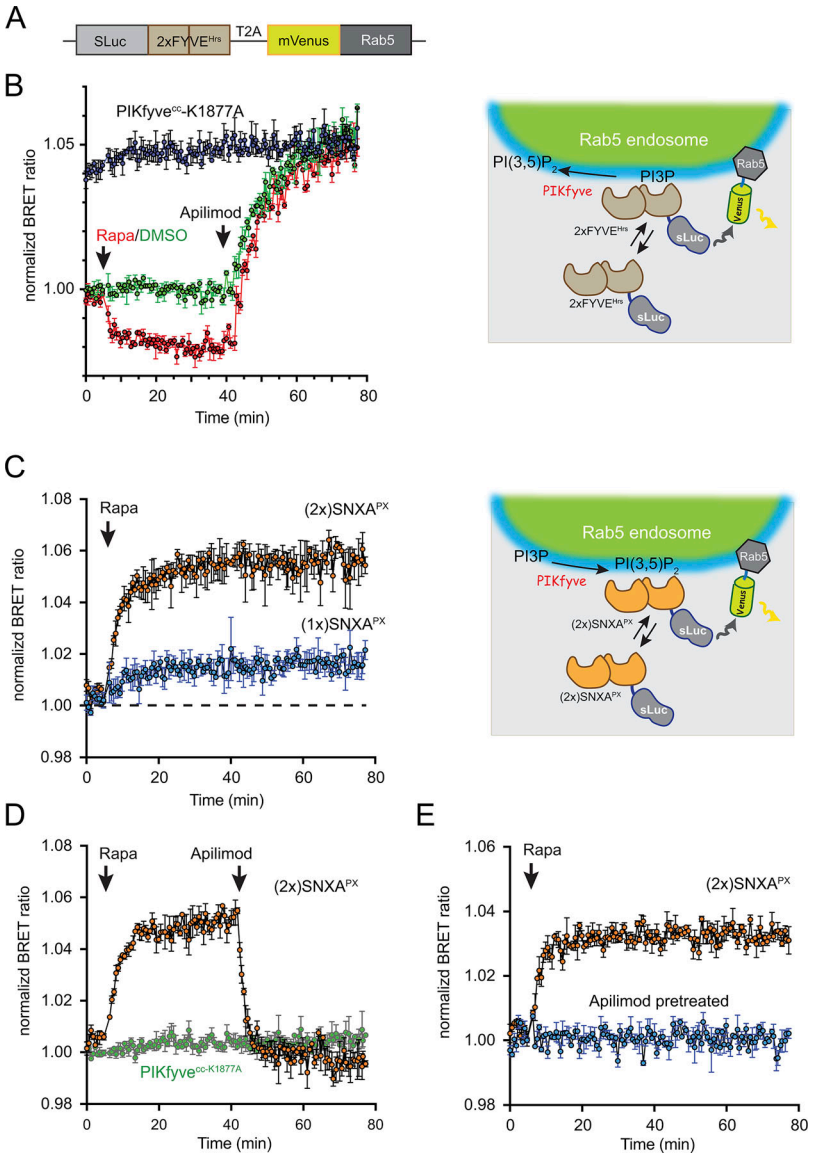

Figure 8. **BRET-based measurements of PI3P and PI(3,5)P_2 changes within Rab5-positive endosomes at the cell population scale. (A)** Cartoon showing the design of the BRET construct used for monitoring PI3P levels in the Rab5-positive endosomes (also see Baba et al. [2019]; Kim et al. [2022]; Pemberton et al. [2020]). **(B)** HEK293A cells were transfected with the high-affinity BRET reporter monitoring PI3P in the Rab5-positive compartments (sLuc-(2x)FYVE^{Hrs}-tPT2A-mVenus-Rab5) together with the iRFP-FRB-Rab5 and either iRFP-FKBP-PIKfyve^{CC} enzyme or a catalytically inactive (K1877A) variant (see Materials and methods for further details and the cartoon presented on the right). BRET values from rapamycin-treated cells were normalized to the identical transfection regime in cells treated only with DMSO. Times of treatment with rapamycin (100 nM) or apilimod (1 µM) are indicated on each trace. Note that the active enzyme (green traces) already decreases PI3P levels compared with cells expressing the inactive version (blue traces), but their PI3P level returns to the same baseline level after apilimod treatment. Recruitment of the FKBP-PIKfyve^{CC} enzyme to Rab5-positive compartments quickly decreases the residual PI3P levels (red traces), while apilimod treatment rapidly reverses these effects. Grand averages (± SEM) are presented from three experiments, with distinct treatments performed in triplicate within each replicate. **(C)** Comparison of the single and tandem *Dd*SNXA^{PX} BRET-based biosensors (see cartoon on the right). BRET measurements were performed as described for B but replacing the (2x)FYVE^{Hrs} domain with either the NES$^{(2x)}$-equipped single (sLuc-*Dd*SNXA^{PX}-tPT2A-mVenus-Rab5) or tandem (sLuc-(2x)*Dd*SNXA^{PX}-tPT2A-mVenus-Rab5) versions of the *Dd*SNXA^{PX} domain in the Rab5-targeted BRET construct. Note the larger total signal obtained with the tandem version of the reporter. Grand averages (± SEM) are presented from three experiments, with distinct treatments performed in triplicate within each replicate. **(D)** BRET-based measurements of PI(3,5)P_2 generation within Rab5-positive compartments in response to the FKBP-PIKfyve^{CC} recruitment using the NES$^{(2x)}$-(2x)*Dd*SNXA^{PX} reporter. Note the rapid reversal of the PI(3,5)P_2 increase after the administration of apilimod and the lack of effects associated with recruitment of the catalytically inactive enzyme. **(E)** Similar experiment showing that pretreatment of cells with apilimod (1 µM, 30 min) completely prevents the ability of the FKBP-PIKfyve^{CC} recruitment to increase the levels of the PI(3,5)P_2 reporter. Grand averages (± SEM) are presented from three experiments, with distinct treatment performed in triplicate within each replicate.

Testing the PI(3,5)P_2-dependent membrane binding of putative PI(3,5)P_2 effectors

Having a tool in hand that can generate sufficient amounts of PI(3,5)P_2 in target membranes, we also tested several putative PI(3,5)P_2-recognizing domains as fusion proteins to mNG, which included (2x)ML1N (Hammond et al., 2015; Li et al., 2013). Among these, testing the tandem (2x)ML1N segment was particularly important as it has been suggested (Li et al., 2013) and used (Hong et al., 2015; Vicinanza et al., 2015) as a PI(3,5)P_2-specific reporter, even if its suitability as such has been questioned (Hammond et al., 2015). As observed earlier (Hammond et al., 2015), EGFP-(2x)ML1N showed some localization to punctate structures, but these did not respond to acute or prolonged apilimod treatment (1 µM; Fig. S5 A). Recruiting the active FKBP-PIKfyve^{CC} enzyme to the Rab5 compartment showed no recognizable increase in the localization of the (2x)ML1N probe to the Rab5 compartment. This was further tested using BRET-based measurements, with (2x)ML1N segment now added as the sLuc-fused reporter (sLuc-(2x)ML1N-tPT2A-mVenus-Rab5), monitoring the local enrichment of the (2x)ML1N domain upon recruitment of the FKBP-PIKfyve^{CC} to Rab5-positive compartments. In this sensitive BRET assay, there was a small but recognizable increase in the measured enrichment of the probe, which was reversed by apilimod treatment (1 µM), suggesting that the (2x)ML1N probe can weakly respond to large increases to PI(3,5)P_2 (Fig. S5 B), but its sensitivity is well below that of the (2x)*Dd*SNXA^{PX} domain. Importantly, however, the visible punctate signal observed with the (2x)ML1N probe did not disappear after apilimod treatment (1 µM; Fig. S5 A), thereby confirming our previous conclusions that the punctate signal

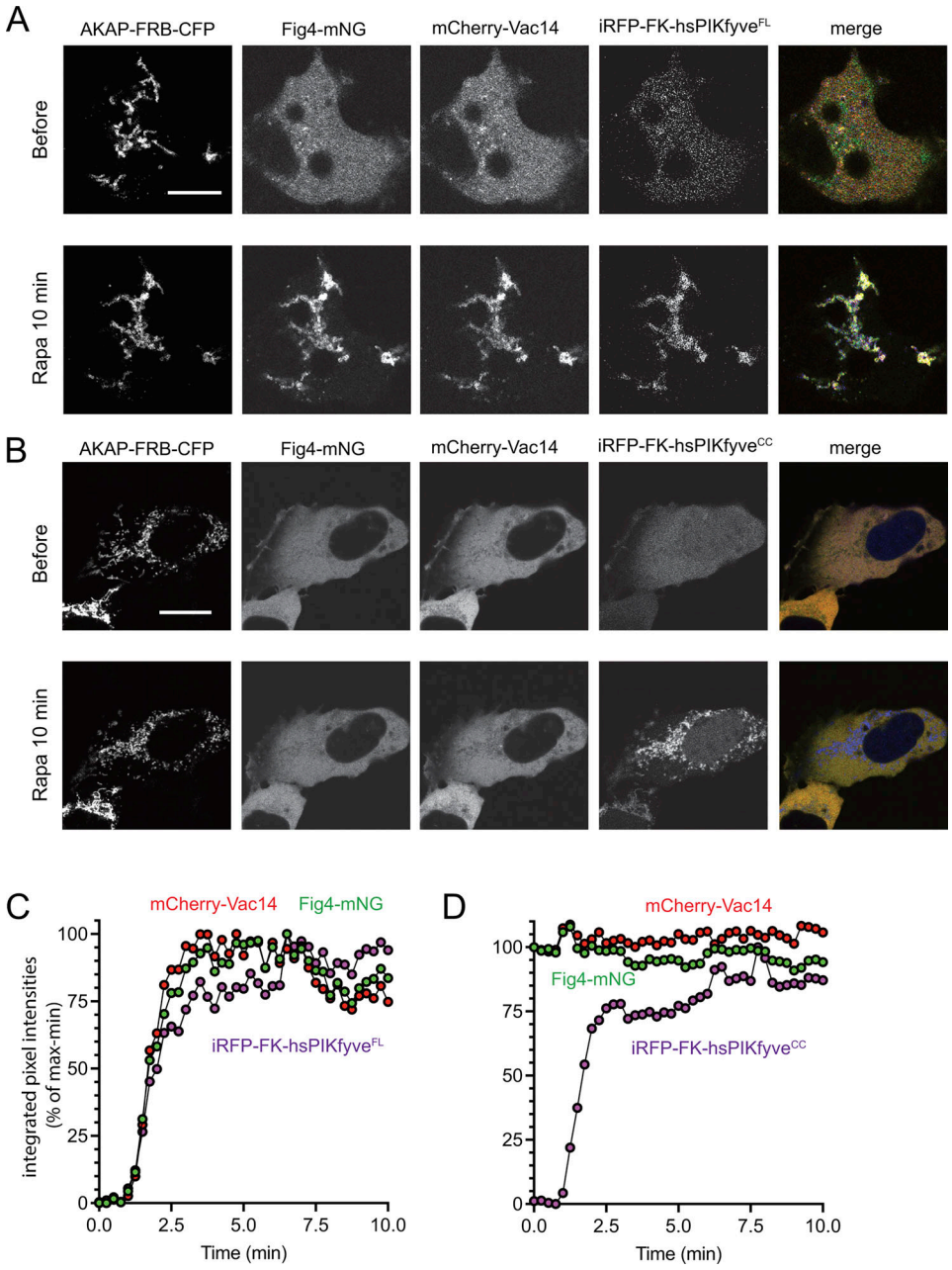

Figure 9. **Unlike full-length PIKfyve, the engineered PIKfyve^{CC} does not associate with the canonical Vac14/Fig4 complex. (A and B)** Rerouting experiments testing the association of the full-length PIKfyve enzyme (A) or the PIKfyve^{CC} fragment (B) with complex-forming molecular partners, Vac14 and Fig4, using confocal imaging. **(A)** Recruitable version of the full-length PIKfyve enzyme (iRFP-FKBP-PIKfyve^{FL}) was co-transfected with mCherry-Vac14 and Fig4-mNG together with an OMM-targeted FRB recruiter (AKAP-FRB-CFP). Rapamycin-induced translocation of FKBP-PIKfyve^{FL} to the mitochondria also caused translocation of Vac14 and Fig4, which is consistent with their association. **(B)** Similar experiment showing the inability of the mRFP-FKBP-PIKfyve^{CC} fragment to co-recruit Vac14 and Fig4 to the OMM. **(C and D)** shows quantification of the mitochondria-associated signal for the individual constructs from A and B, respectively. These results were reproduced four times. For details of quantification, see Materials and methods (scale bars = 10 µm).

detected by the (2x)ML1N construct in resting cells cannot be attributed to PI(3,5)P_2 (Hammond et al., 2015).

Discussion

Here, we present the design and characterization of an engineered minimal catalytic fragment of the human PIKfyve enzyme for the acute and controlled production of the enigmatic lipid, PI(3,5)P_2, in subcellular membrane compartments. Our alternative approaches to generating an active PIKfyve fragment were originally focused on using just the C-terminal segment of the enzyme that was resolved in prior structural descriptions (Lees et al., 2020). However, these initial efforts were unsuccessful and only the final design that we describe here, which removes the large and unstructured inter-domain loops, but retains the short linker sequence (1384–1404) that runs alongside

the presumptive substrate-binding pocket, ultimately proved to be functional as a highly active PIKfyve^{CC}. While several putative PI(3,5)P_2-binding effectors have been already described (see the Introduction for references), these prior studies have lacked the required molecular tools to properly evaluate these probes as truly lipid-specific PI(3,5)P_2 reporters in live cells (Hammond et al., 2022). The ability to acutely increase the cellular levels of PI(3,5)P_2 in specific membrane compartments is an important step forward to test the validity of any putative PI(3,5)P_2 probes. Indeed, the recent identification of the PX domain of *Dd*SNXA as a selective PI(3,5)P_2 sensitive reporter (Maib et al., 2024; Vines et al., 2023) was a major breakthrough. However, as we now show, even an optimized reporter based on the *Dd*SNXA fails to decorate any membranous structures in many cell types when expressed in live cells, which is likely due to the extremely small amount of available PI(3,5)P_2 to present in the cytoplasmic leaflets of subcellular organelles. That said, the expression of the catalytically active PIKfyve^{CC} fragment allowed for the further characterization of the *Dd*SNXA^{PX} as a useful PI(3,5)P_2 reporter. Results using localized recruitment of the FKBP-PIKfyve^{CC} effectively confirm the reported specificity for PI(3,5)P_2, while also establishing the sufficiency of PI(3,5)P_2 recognition for the membrane residency of this probe.

Our BRET analysis showed the largest PI(3,5)P_2 signal upon recruitment of the PIKfyve^{CC} fragment to Rab5-positive compartments, which are known to have high resting levels of PI3P. The sustained elevation of the *Dd*SNXA^{PX} signal observed in the BRET analysis when PI(3,5)P_2 was generated in Rab5-positive compartments, as well as the rapid reversibility of this enrichment after apilimod treatment, suggests that the PI3P supply in these membranes can keep up with the higher local conversion to PI(3,5)P_2. In addition, the activity of the recruited FKBP-PIKfyve^{CC} must outpace the elimination of PI(3,5)P_2 by resident enzymes that can promote its clearance, which are most likely Fig4 and other myotubularin family lipid phosphatases. However, the fact remains that the resting levels of PI(3,5)P_2 are kept exceedingly low, and consequently, the activity of the kinase must be tightly regulated.

It is important to emphasize that the active catalytic PIKfyve fragment will generate extra PI(3,5)P_2 in cellular compartments where its substrate, PI3P, is present, such as the Rab5 compartment. This, however, does not mean that the endogenous PI(3,5)P_2 is present at its highest levels in the entire Rab5 compartment as clearly shown by the distribution of the *Dd*SNXA^{PX} reporter without the expression of the active PIKfyve fragment in our derived HEK293-AT1 cells. In these cells, the high-avidity (2x)*Dd*SNXA^{PX} variant of this reporter localized to a vesicular compartment, which was clearly distinct from Rab5 endosomes. The probe showed clear associations with a small fraction of the Rab7 compartment and only a fraction of the LAMP1-positive endosomes. The most acidic LysoTracker–positive small vesicles did not show PI(3,5)P_2 enrichment. Notably, some PI(3,5)P_2-positive membranes were also detected in the lumen of enlarged lysosomes in some cells. It is worth noting that the (2x)*Dd*SNXA^{PX} signal was completely eliminated after apilimod treatment and also after treatment with the Vps34 inhibitor, IN1. This suggests that endogenous PIKfyve largely utilizes PI3P generated by the Vps34 enzyme. These localization data are in good agreement with the localization data of endogenously tagged PIKfyve, which was found to only partially co-localize with EEA1- and Rab7-positive endosomes, but showed the highest co-localization with Vps35 (Giridharan et al., 2022). Our data are also in good agreement with those presented in a recent study that used a recombinant *Dd*SNXA^{PX}-based reporter together with super-resolution imaging of fixed cells (Maib et al., 2024), although these authors did find PI(3,5)P_2-positive signal overlapping with presumably Rab5-positive, PI3P-containing endosomes.

Our data clearly support the conclusion that the engineered PIKfyve^{CC} fragment is highly active when expressed in cells, suggesting potential hyperactivation compared with full-length PIKfyve. The only molecular insight into the regulation of PIKfyve is from the medium-resolution cryo-EM structure of it bound to its regulatory partners Vac14 and Fig4 (Lees et al., 2020). This structure was not of sufficient resolution to build a complete atomic model of PIKfyve, preventing full interpretation of how regulatory domains modulate PIKfyve activity. AlphaFold modeling predicted that the CCT/CCR domains form an interface with the C-lobe of the kinase domain, and the 3HB domain forms an interface with the N-lobe of the kinase domain, with our HDX-MS results now supporting the secondary structure predicted by this model. Intriguingly, the CCT/CCR domains are linked to the 3HB through a linker region that directly interacts with the C-lobe of the kinase domain, with the linker mimicking the conformation of an insertion present in the evolutionarily similar PI5P4Ks and PI4P5Ks (Hu et al., 2015; Sumita et al., 2016). HDX-MS analysis of the engineered PIKfyve^{CC} fragment bound to membranes revealed disruption of the interface between this linker and the surrounding kinase domain. Overall, this is indicative of the linker acting as a possible regulatory mechanism, with interactions between the kinase domain and the CCT/CCR domains and the 3HB domain altering the dynamics of this linker region. Dominant-active mutants were identified in Fab1, which were predicted to alter an inhibitory interface with the CCR/CCT domains. The majority of these mutants are present in helix 2250–2264 in Fab1 (equivalent to helix 2069–2083 in human PIKfyve), which is part of the predicted interface with the CCR/CCT domains. Disruption of this segment would likely weaken the interface between the kinase domain and the linker region. The dynamics of this interface may also play a critical role in allowing the active site of PIKfyve to interact with the lipid substrate, as the PIKfyve active site was predicted to be unable to bind membranes in the PIKfyve/Vac14/Fig4 complex (Lees et al., 2020), and disengagement of the kinase domain may allow it to adapt a conformation able to bind membranes. This would be similar to large-scale conformational changes of the kinase domain of Vps34 relative to other domains predicted to be required for engagement with the lipid substrate (Stjepanovic et al., 2017). Further investigations on how the regulatory domains of PIKfyve regulate lipid kinase activity will be critical in further exploitation of engineered

PIKfyve constructs as tools, and development of therapeutics targeting PIKfyve.

Lastly, an exciting new opportunity offered by these tools is the ability to rapidly increase $PI(3,5)P_2$ levels within specific subcellular compartments and monitor the activities of specific molecular effectors or biological processes. Some of these exciting studies are already in progress within our group, and how such tools can contribute to the evaluation of cellular responses that are potentially controlled by $PI(3,5)P_2$ metabolism is also demonstrated in an accompanying study in this issue (Wu et al., 2025). However, we must mention that one of the caveats associated with the use of these tools is the high basal activity of the PIKfyve^{CC} fragment from the cytoplasm. Current efforts in our group are focused on modifying the membrane-interacting surface of the enzyme to lower its activity from the cytosol, while still retaining its strong catalytic activity when acutely recruited to subcellular membranes. Unfortunately, these approaches have proven to be extremely challenging due to the apparent instability of the folded domain in response to even subtle modifications of the current PIKfyve^{CC} backbone, including point mutations. Nonetheless, the high activity observed for the engineered PIKfyve^{CC} also suggests that the activity of the endogenous PIKfyve must be tightly controlled, likely through autoinhibitory interactions within the PIKfyve polypeptide itself and, as already demonstrated in elegant previous studies (Lang et al., 2017), by contacts with binding partners, including both Vac14 and Fig4. Taken together, these novel tools, as well as the ongoing efforts to improve them, will help us better understand the complex regulation of PIKfyve-mediated catalysis and allow for new investigations exploring the molecular targets and cellular processes that are dynamically controlled by $PI(3,5)P_2$.

Materials and methods

Cell culture

HEK293A (Invitrogen) or HEK293-AT1 cells, which stably express the rat AT_{1a} angiotensin II receptor (Hunyady et al., 2002), were cultured in Dulbecco's modified Eagle's medium (DMEM—high glucose; Gibco, Life Technologies) containing 10% (vol/vol) FBS and supplemented with a 1% solution of penicillin–streptomycin (Gibco, Life Technologies). Cell lines were maintained at 37°C and 5% CO_2 in a humidified atmosphere and regularly tested for *Mycoplasma* contamination using a commercially available detection kit (InvivoGen). Furthermore, after thawing, cell cultures are treated with Plasmocin (InvivoGen) at 500 µg/ml for the initial three passages (6–9 days) and then supplemented with 5 µg/ml of the prophylactic for all subsequent passages.

Reagents

All compounds were prepared in the indicated solvent and stored in small aliquots at −20°C. Rapamycin (100 µM stock; Sigma Millipore) and apilimod (1 mM stock; Selleck Chemicals) were dissolved in DMSO. Coelenterazine h (Regis Technologies) was dissolved in 100% ethanol (vol/vol) and stocked at 5 mM. LysoTracker Red was from Thermo Fisher Scientific.

DNA constructs for mammalian expression

Plasmids were constructed by standard restriction cloning using enzymes from New England Biolabs, while site-directed mutagenesis was done using the QuikChange II kit (Agilent). Complex reconfigurations of vector backbones and all point mutations were verified using standard Sanger sequencing (Psomagen). The design of the following plasmids has been described elsewhere: mCherry-Rab5, mCherry-Rab7, LAMP1-mCherry (Jović et al., 2014; Jovic et al., 2012), OMM-FRB-ECFP (Csordás et al., 2010), iRFP-FRB-Rab5 (Plasmid #51612; Addgene) (Hammond et al., 2014), mRFP-FKBP12-5-ptase domain (Varnai et al., 2006), iRFP-FKBP-*Bc*PI-PLC^{AA} (Pemberton et al., 2020), sLuc-(2x)FYVE^{Hrs}-T2A-mVenus-Rab5 (Pemberton et al., 2020), EGFP-ML1Nx2 (Li et al., 2013), pLX304-VAC14 (*Homo sapiens*; DNASU Plasmid #HsCD00443610), and pANT7-cGST-FIG4 (*H. sapiens*; DNASU Plasmid #HsCD00859243). We also thank the laboratories of Geert van den Bogaart (Radboud Institute for Molecular Life Sciences, Nijmegen, the Netherlands) (pEGFP-PIKfyve; Plasmid #121148; Addgene) (Baranov et al., 2019), Michael Davidson & Vladislav Verkhusha (Albert Einstein College of Medicine, New York, NY, USA) (piRFP-N1; Plasmid #54787; Addgene) (Filonov et al., 2011), and Isei Tanida (Juntendo University School of Medicine, Tokyo, Japan) (pmNG^{HO}-G-C1; Plasmid #127912; Addgene) for generously providing plasmids. The cloning procedures used for generating the constructs that are unique to this study are provided below, and the primers required for either PCR amplification or site-directed mutagenesis are listed in Table S1.

The truncated PIKfyve^{CC} insert was comprised of residues 1383–1522, 1629–1706, and 1796–2098 of Human PIKfyve (UniProt ID: Q9Y2I7), and custom-synthesized (GeneArt Strings DNA Fragments; Thermo Fisher Scientific) with short G-rich linkers added at the inter-domain boundaries. The complete sequence of the synthesized PIKfyve^{CC} insert was as follows: 5′-CGATCGAGC
CCCATCAGACTGCTGGAAGTCTGTGTGCCCCTGCCTAAGATTTT
CATCAAGCGGCAGGCCCCTCTGAAAGTGTCACTGCTGCAGGACC
TGAAGGACTTCTTCCAGAAAGTGTCCCAGGTGTACGTGGCCAT
CGACGAGAGACTGGCCAGCCTGAAAACCGACACCTTCAGCAAG
ACCCGGGAAGAGAAGATGGAAGATATTTTCGCCCAGAAAGAAA
TGGAAGAGGGCGAGTTCAAGAACTGGATCGAGAAGATGCAGGC
CCGGCTGATGAGCAGCTCTGTGGATACACCTCAGCAGCTGCAG
TCCGTGTTCGAGAGCCTGATCGCCAAGAAACAGAGCCTGTGCG
AAGTGCTGCAGGCTTGGAACAACCGGCTGCAGGATCTGTTCCA
GCAAGAGAAGGGCAGAAAGAGGCCTTCTGGCGGCGGAGGATC
TGCCAATCTGCTGCCTGGCAACAGCTACAACCCCATTCCTTTT
CCATTCGACCCCGACAAGCACTACCTGATGTACGAGCACGAG
CGGGTGCCAATCGCCGTGTGCGAGAAAGAGCCCAGCAGCATC
ATTGCCTTCGCTCTGAGCTGCAAAGAGTACCGGAACGCCCTGG
AAGAACTGAGCAAGGCCACACAGTGGAACAGCGCCGAAGAGG
GCCTGCCTACCAATTCTACATCTGGCGGAGGCGGAGGGGACAC
CCAGAAGAAGCAACTGATCAACCCTCACGTCGAGCTGCAGTTC
AGCGACGCCAACGCCAAGTTCTACTGCCGGCTGTATTACGCCG
GCGAGTTCCACAAGATGCGGGAAGTGATCCTGGACAGCAGCGA
AGAGGACTTCATCAGAAGCCTGAGCCACAGCTCTCCATGGCAG
GCCAGAGGTGGAAAAAGCGGAGCCGCCTTTTACGCCACCGAGG
ACGACAGATTCATCCTGAAGCAGATGCCCCGGCTGGAAGTGCA
GAGCTTCCTGGATTTTGCCCCTCACTACTTCAACTACATCACCA

ACGCCGTGCAGCAGAAGAGGCCAACAGCTCTGGCCAAGATCC
TGGGCGTGTACCGGATCGGCTACAAGAACAGCCAGAACAATAC
CGAGAAGAAACTGGACCTGCTGGTCATGGAAAACCTGTTCTACG
GCCGGAAGATGGCCCAGGTGTTCGATCTGAAGGGCAGCCTGCG
GAACCGGAACGTGAAAACAGATACCGGCAAAGAAAGCTGCGA
CGTGGTGCTGCTGGACGAGAACCTGCTGAAGATGGTCCGAGAC
AACCCTCTGTATATCCGCAGCCACAGCAAGGCCGTGCTGAGAA
CCAGCATCCACAGCGACAGCCACTTTCTGAGCAGCCACCTGAT
CATCGACTACAGCCTGCTCGTGGGCAGAGATGACACCAGCAAT
GAGCTGGTCGTGGGCATCATCGATTACATCAGAACCTTCACG
TGGGACAAAAAGCTGGAAATGGTGGTCAAGAGCACCGGCATCC
TCGGCGGACAGGGAAAGATGCCTACAGTGGTGTCTCCCGAGCT
GTACCGGACCAGATTTTGCGAGGCTATGGACAAGTACTTTCTG
ATGGTGCCCGACCACTGGACAGGCCTGGGACTGAATTGCTGAG
GATCC-3′. The engineered PIKfyve^{CC} insert was then amplified from the human codon–optimized DNA fragment and inserted in place of the type IV 5-phosphatase domain in mRFP-FKBP12-5-ptase using a PvuI/BamHI double digest to generate the mRFP-FKBP-PIKfyve^{CC}. To alleviate any concerns related to potential interference with BRET-based measurements, we also made the iRFP-FKBP-PIKfyve^{CC} by replacing mRFP with the iRFP module from iRFP-FKBP-*Bc*PI-PLC^{AA} using NheI and BspEI restriction sites. Site-directed mutagenesis of the mRFP- or iRFP-tagged FKBP-PIKfyve^{CC} backbones was then used to generate the K1877A catalytically inactive controls.

To facilitate the diverse cloning strategies needed for the biosensor designs used in this study, the PX domain (residues 61–175) from the *D. discoideum (Dd)* SNXA (*Dd*SNXA; DDB_G0289833; UniProt ID: Q54GY1) was codon-optimized for mammalian expression and custom-synthesized (GeneArt Strings DNA Fragments; Thermo Fisher Scientific) in the tandem orientation ((2x)*Dd*SNXA^{PX}) with a flexible (GGGGS)x3 leader sequence at the N terminus and (SAGG)x4 inter-domain linker between the *Dd*SNXA^{PX} segments. The complete sequence of the synthesized (2x)*Dd*SNXA^{PX} insert was as follows: 5′-ATA
TATTCCGGAAGATCTCGATCGTCCGGCGGAGGCGGATCTGGT
GGCGGAGGAAGTGGCGGCGGAGGTAGAGCACAAGCTTCGGAA
ATCTACATCACCGTGCCTCGGAAGATCCAGGGCGAAGAGGGC
CTGATGAGAAAGTACACCGCCTACGTGATCGAGGTGGAAGGC
AGCGAGAACAAGAGATACCAAGTGACCCGGCGGTACAAGCAG
TTCGTGCTGCTGCATACCCAGCTCGTCAGAGTGTTCGGCGAG
CACGATCTGCCTTCTCTGCCTGCCAAAGCCAACGGCCTGTAC
TTCAGCAAGGACGACCACACCGAGAAGCGGAGAGTGAACCTG
CAAGAGTACCTCCAGAACCTGGCCAAGAATCCCGCCATCCTG
AACAGCCCCGTGTTCTACCACTTCCTGAAGAGAGATGAGGGC
CAGAACTCTCGAGGATCTGCCGGTGGTTCTGCTGGTGGAAGT
GCTGGCGGTTCAGCTGGCGGCTCGAATTCTGAAATCTATATT
ACAGTGCCCCGCAAAATTCAAGGCGAAGAGGGACTCATGCGG
AAGTATACAGCCTATGTGATTGAAGTCGAGGGCTCCGAGAAC
AAACGGTATCAAGTGACAAGACGCTATAAGCAGTTTGTCCTG
CTCCACACGCAACTTGTTCGCGTGTTCGGAGAACATGACCTG
CCTAGCCTGCCAGCCAAGGCTAATGGACTGTACTTTTCCAAG
GATGATCACACAGAGAAACGGCGGGTCAACCTCCAAGAATAC
CTGCAAAATCTGGCTAAAAACCCGGCCATTCTGAACTCC
CCAGTCTTTTACCATTTTCTCAAACGCGACGAGGGGCAGAAC
GTCGACTAAGGTACCATATAT-3′. Unique flanking and internal restriction sites allowed for the assembly of both the single domain or tandem (2x) *Dd*SNXA^{PX} variants as either standard mNG^{HO}-fusion proteins or BRET constructs. Briefly, using the pmNG^{HO}-C1 empty vector, an XhoI/KpnI double digest would allow for insertion of the isolated *Dd*SNXA^{PX} sequence (mNG^{HO}-*Dd*SNXA^{PX}), while digestion with BspEI/KpnI would assemble the tandem mNG^{HO}-(2x)*Dd*SNXA^{PX}. To generate the NES-mNG^{HO}-(2x)*Dd*SNXA^{PX} variant, the NES-flanked $^{(2x)NES}$mNG^{HO} insert was generated by amplifying the existing mNG^{HO} using primers with an overhanging NES at both the N (NES #1: ALQKKLEELELDE) and C termini (NES #2: LPPLERLTL), which was then exchanged for the existing fluorophore using NheI and BspEI restriction sites.

Alternatively, using sLuc-(2x)FYVE^{Hrs}-T2A-mVenus-Rab5, an XhoI/SalI double digest would replace the (2x)FYVE^{Hrs} module with the isolated *Dd*SNXA^{PX} sequence (sLuc-*Dd*SNXA^{PX}-T2A-mVenus-Rab5), while digestion with BglII/SalI would assemble the tandem sLuc-(2x)*Dd*SNXA^{PX}-T2A-mVenus-Rab5 biosensor. Generation of sLuc-ML1Nx2-T2A-mVenus-Rab5 used a similar strategy, with replacement of (2x)FYVE^{Hrs} in sLuc-(2x)FYVE^{Hrs}-T2A-mVenus-Rab5 after amplification from the EGFP-(2x)ML1N vector and a BglII/SalI double digest. For each of these Rab5-targeted BRET biosensors, the single T2A site was exchanged for a tandem tPT2A (Liu et al., 2017), which was amplified from a short synthetic DNA fragment (gBlocks; Integrated DNA Technologies), using SalI and AgeI restriction sites. Additionally, the sLuc was exchanged for NES-sLuc by adding the same N- (NES #1: ALQKKLEELELDE) and C-terminal (NES #2: LPPLERLTL) NES overhangs described previously during PCR amplification and then using NheI and BglII restriction sites in the shared sLuc-(X)-tPT2A-mVenus-Rab5 backbone.

Finally, for the enzyme rerouting studies, we generated an FKBP-tagged full-length Human PIKfyve (mRFP-FKBP-PIKfyve^{FL}) by replacing the EGFP module in EGFP-hPIKfyve (# 121148; Addgene) with an amplified mRFP-FKBP12 segment from an existing recruitable enzyme backbone together with an NheI/SalI double digest. To visualize the assembly of the larger PIKfyve complex, mNG^{HO}-Vac14 was first made by amplifying the Human Vac14 coding sequence from pLX304-VAC14 (*H. sapiens*; DNASU Plasmid #HsCD00443610) and inserting this into the mNG^{HO}-C1 empty vector using a HindIII/SalI double digest. Next, to create Fig4-iRFP, the human Fig4 coding sequence was amplified from pANT7-cGST-FIG4 (*H. sapiens*; DNASU Plasmid #HsCD00859243) and inserted into the iRFP-N1 empty vector using NheI and AgeI restriction sites.

Live-cell confocal microscopy

For imaging studies, HEK293A or HEK293-AT1 cells (3 × 10^5 cells/dish) were plated with a final volume of 1.5 ml on 29-mm circular glass-bottom culture dishes (#1.5; Cellvis) precoated with 0.01% poly-L-lysine solution (Sigma-Aldrich). Cells were allowed to attach overnight prior to transfection with plasmid DNAs (0.1–0.2 µg/well) using Lipofectamine 2000 (2–5 µl/well; Invitrogen) within a small volume of Opti-MEM (200 µl; Invitrogen). Media containing the Lipofectamine-complexed DNA were replaced at 4–6 h after transfection with complete culture medium. In general, cell densities were always kept between

50% and 80% confluence for the day of imaging. Also, studies using the rapamycin-inducible protein heterodimerization system used a 1:2:1 ratio of plasmid DNA for transfection of the FKBP-tagged enzyme (0.1 µg), FRB-labeled recruiter (0.2 µg), and indicated protein or biosensor of interest (0.1 µg; total DNA: 0.4 µg/well). After 18–20 h of transfection, cells were incubated in 1 ml of the modified Krebs–Ringer solution (containing 120 mM NaCl, 4.7 mM KCl, 2 mM $CaCl_2$, 0.7 mM $MgSO_4$, 10 mM glucose, 10 mM HEPES, and pH adjusted to 7.4) and images were acquired at room temperature using a Zeiss LSM 880 (63×/1.40 N.A. Plan-Apochromat Oil DIC M27 Objective) laser-scanning confocal microscope (Carl Zeiss Microscopy). Image acquisition was performed using the ZEN software system (Carl Zeiss Microscopy), while image preparation and analysis was done using the open-source FIJI platform (Schindelin et al., 2012). Only linear adjustments to the displayed dynamic range were allowed, and all of the representative images shown are of HEK293 lineage cells.

Image analysis

Image quantification was performed using FIJI (ImageJ, version: 2.14.0/1.54 m) software. For single transfections, the image was thresholded and the integrated pixel intensities were calculated for the entire time-lapse sequence. When applicable, multiple cells were quantified and the values were normalized to the starting values, taken as 100%. In some cases, where photobleaching was significant, the bleach-correction function was used. For multiple transfections, where an organelle marker could be used as a mask after thresholding, the individual integrated pixel intensities were calculated for each individual channel using the mask as the template. In the mitochondrial co-recruitment experiments, several recordings of individual cells obtained in separate transfections were analyzed, and the kinetics of the individual channels was plotted as a fraction of the difference between the minimum and maximum average pixel intensity values. In the case of co-localization of the PI(3,5)P_2 reporter with the various endosomal compartments, z-stacks were used for the co-localization analysis and the co-localization was calculated for each section. Here, a mask was generated using the thresholded PI(3,5)P_2 reporter image and used to calculate the average pixel intensities of the background-subtracted endosomal marker image in that mask throughout the z-planes. These values were then divided by the respective average pixel intensity values obtained for the entire thresholded endosomal marker throughout the z-planes. This analysis allowed for the best estimate of the co-localization of the PI(3,5)P_2 reporter with only a small fraction of the different endosomal markers.

Kinetic measurements of membrane PI(3,5)P_2 content using BRET-based reporters

BRET measurements were made at 37°C using TriStar2 LB 942 Multimode Microplate Reader (Berthold Technologies). HEK293A cells (0.75×10^5 cells/well) were seeded in a 200 µl total volume to white-bottom 96-well plates precoated with 0.01% poly-L-lysine solution (Sigma-Aldrich) and cultured overnight. Cells were then transfected with 0.25 µg of the specified BRET biosensor using Lipofectamine 2000 (1 µl/well) within Opti-MEM (40 µl); once again, the media containing the Lipofectamine-complexed DNA were replaced with complete culture medium at between 4 and 6 h after transfection. Components of the rapamycin-inducible heterodimerization system were transfected together with the BRET biosensor at an empirically determined ratio of 1:1:5 for the FRB (0.05 µg), FKBP (0.05 µg), and BRET (0.25 µg) constructs, respectively (0.35 µg/well in total). Between 20 and 24 h after transfection, the cells were quickly washed before being incubated for 30 min in 50 µl of the modified Krebs–Ringer buffer (containing 120 mM NaCl, 4.7 mM KCl, 2 mM $CaCl_2$, 0.7 mM $MgSO_4$, 10 mM glucose, 10 mM HEPES, and pH adjusted to 7.4) at 37°C in a CO_2-independent incubator. After the preincubation period, the cell-permeable luciferase substrate, coelenterazine h (40 µl, final concentration 5 µM), was added and the signals from the mVenus fluorescence and sLuc luminescence were recorded using 485- and 530-nm emission filters over a 4-min baseline BRET measurement (30 s/cycle). Following the baseline recordings, where indicated, the plates were quickly unloaded for the addition of various treatments, which were prepared in a 10 µl vol of the modified Krebs–Ringer solution and added manually. Detection time was always 500 ms for each wavelength, and measurements were initiated at the 0-min demarcation indicated on all graphs and continued for 60 min (30 s/cycle) after the addition of any treatments. All measurements were carried out in triplicate wells and repeated in three independent experiments. From each well, the BRET ratio was calculated by dividing the 530- and 485-nm intensities, which were then normalized to the baseline measurement. In order to facilitate the pooling of data from individual wells and between replicate experiments, the raw BRET ratios were processed using a simple moving average with a four-cycle interval across the BRET kinetic. The processed BRET ratios obtained from drug-treated wells were then normalized to internal vehicle controls. Additionally, where indicated, values obtained for the same BRET biosensor from experiments using multiple recruitable enzymes or different FRB-tagged recruiters were also normalized to control measurements made simultaneously using the corresponding catalytically inactive enzyme variants.

AlphaFold3 modeling

We used the protein prediction software, AlphaFold3 (Abramson et al., 2024), to model the structure of PIKfyve bound to a dimer of Vac14 and Fig4, the pentameric complex of Vac14 bound to Fig4, and the PIKfyve^{CC} construct. For each input, AlphaFold generated five models ranked in order by mean pLDDT. The predicted aligned error for these models is shown in Fig. S1. All domains that showed no inter-domain contacts were removed from the model in Fig. 1 A. To generate a model of the PIKfyve^{CC}, we removed all truncated residues from the model shown in Fig. 1 A. This was used for HDX-MS color mapping and main text figures. PDB models generated from these searches are included as PDB files in the source data, with residues having Cα pLDDT <50 being removed.

Table 1. **Methods resources used in this study**

Reagent or resource	Source	Identifier
Bacterial and virus strains		
E. coli XL10-GOLD KanR ultracompetent cells	Agilent	200317
E. coli DH10EMBacY competent cells	Geneva Biotech	DH10EMBacY
Chemicals, peptides, and recombinant proteins		
Deuterium oxide 99.9%	Sigma-Aldrich	151882-10X1ML
ATP	Sigma-Aldrich	A7699-1g
Protease inhibitor cocktail	Sigma-Aldrich	535140
Polyoxyethylene (10) lauryl ether	Sigma-Aldrich	P9769
Phosphatidylserine (porcine brain)	Avanti	840032C
Phosphatidylethanolamine (egg yolk)	Sigma-Aldrich	P6386
Phosphatidylcholine (egg yolk)	Avanti	840051C
PI3P (synthetic)	Avanti	850150-500UG
Polyethanolamine	Polysciences	24765
Critical commercial assays		
Transcreener ADP2 FI assay (1,000 Assay, 384 Well),	BellBrook Labs	3013-1K
Recombinant DNA		
PIKfyve^{CC} construct (pLIB)	This paper	MJ290
Software and algorithms		
HDExaminer	Sierra Analytics	http://massspec.com/hdexaminer
GraphPad Prism 7	GraphPad	https://www.graphpad.com
Adobe Illustrator	Adobe	https://www.adobe.com/products/illustrator.html
PyMOL	Schroedinger	http://pymol.org
Other		
Sf9 insect cells for expression	Expression Systems	94-001S

Plasmid generation for recombinant protein production

The engineered PIKfyve^{CC} (1383–1522, 1629–1706, and 1796–2098; see the exact sequence above) construct was inserted into the pLIB vector to allow baculovirus expression in *Spodoptera frugiperda* (Sf9) cells. The full list of all plasmids and reagents utilized in this manuscript is shown in the methods resources table (Table 1). The plasmid containing the PIKfyve core expressed N terminus to the protein a 10X histidine tag, followed by a 2X Strep tag, followed by a tobacco etch virus protease cleavage site.

Virus generation and amplification

The plasmid harboring the PIKfyve^{CC} was transformed into DH10MultiBac cells (MultiBac; Geneva Biotech) containing the baculovirus viral genome (bacmid) and a helper plasmid expressing transposase to transpose the expression cassette harboring the gene of interest into the baculovirus genome. Bacmids with successful incorporation of the pLIB expression cassette into the viral genome were identified by blue-white screening and purified from a single white colony using a standard isopropanol–ethanol extraction method. Briefly, colonies were grown overnight (~16 h) in 3–5 ml 2xYT (#SD7019; BioBasic). Cells were pelleted by centrifugation, and the pellet was resuspended in 225 µl P1 buffer (MiniPrep Kit, #27106; Qiagen) and chemically lysed by the addition of 225 µl Buffer P2, and the lysis reaction was neutralized by the addition of 300 µl Buffer N3. Following centrifugation at 21,130 rcf and 4°C (#5424 R; Rotor), the supernatant was separated and mixed with 600 µl isopropanol to precipitate the DNA out of solution. Further centrifugation at the same temperature and speed pelleted the bacmid DNA, which was then washed with 500 µl 70% ethanol three times. The bacmid DNA pellet was then dried for 1 min and resuspended in 50 µl Buffer EB.

Purified bacmid was then transfected into Sf9 cells. 2 ml of Sf9 cells between 0.3 and 0.5 × 10^6 cells/ml was aliquoted into the wells of a 6-well plate and allowed to attach, creating a monolayer of cells at ~70–80% confluency. Transfection reactions were prepared by the addition of 2–10 µg of bacmid DNA to 100 µl 1xPBS and 12 µl polyethyleneimine (PEI) at 1 mg/ml (PEI "Max" MW 40,000, #24765; Polysciences) to 100 µl 1xPBS. The bacmid/PBS and the PEI-PBS solutions were mixed, and the reaction occurred for 20–30 min before drop-by-drop addition to an Sf9 monolayer–containing well. Transfections were allowed to proceed for 5–7 days before harvesting the virus-containing supernatant as a PI viral stock.

Viral stocks were amplified by adding P1 viral stock to suspension Sf9 cells between 1 and 2 × 10^6 cells/ml at a 0.01 vol ratio. This amplification produces a P2 stage viral stock that can be used in final protein expression. The amplification proceeded for 4–5 days before harvesting, with cell shaking at 120 RPM in a 27°C shaker (New Brunswick). Harvesting of P2 viral stocks was carried out by centrifuging cell suspensions in 50-ml Falcon tubes at 2281 RCF (GS15; Beckman), collecting the supernatant in a fresh sterile tube, and adding 5–10% inactivated FBS (#97068-085; VWR).

Expression and purification of recombinant proteins

The PIKfyve^{CC} was expressed using the baculovirus expression system in Sf9 cells. After expressing the cells at 27°C for 68 h, the cells were harvested at 1,739 × *g* at 4°C using Eppendorf Centrifuge 5810R and the cells were flash-frozen using liquid nitrogen and stored at −80°C. The frozen pellets were resuspended in lysis buffer containing 20 mM Tris, pH 8, 10 mM imidazole, pH 8, 100 mM NaCl, 5% glycerol (vol/vol), 2 mM βME, and protease inhibitor (Protease Inhibitor Cocktail Set III; Sigma-Aldrich), and sonicated for 2 min (15 s on, 15 s off, level 4.0, Misonix Sonicator 3000). Triton X-100 was added to the lysate at a final concentration of 0.1% and then clarified by spinning at 15,366 × *g* for 45 min (JA-20 rotor; Beckman Coulter). The supernatant was loaded onto a 5-ml crude Ni-NTA column (GE Healthcare) equilibrated in Ni-NTA A buffer (20 mM Tris, pH 8,

100 mM NaCl, 10 mM imidazole, and 5% glycerol [vol/vol]). The column was washed using high salt buffer (20 mM Tris, 1 M NaCl, 10 mM imidazole, 5% Glycerol [vol/vol]) followed by Ni-NTA A buffer wash and 6% Ni-NTA B wash (20 mM Tris, pH 8, 100 mM NaCl, 250 mM imidazole, and 5% glycerol). The protein was eluted using 100% Ni-NTA B buffer, and the elute from the nickel column was loaded onto a 5-ml StrepTrap HP column (GE Healthcare) equilibrated in gel filtration buffer (GFB) (20 mM Tris, pH 7, 100 mM NaCl, 5% glycerol, and 0.5 mM tris(2-carboxyethyl) phosphine), and subjected to buffer wash using GFB. The column was incubated on ice for 18 h in the presence of TEV protease and then eluted by a wash with GFB. The eluent was concentrated in 30,000 MWCO Amicon Concentrator (Millipore) to <1 ml and injected into a Superdex 200 10/300 GL Increase size-exclusion column (GE Healthcare) equilibrated in GFB. After gel filtration, the protein was concentrated to 2 mg/ml using 30,000 MWCO Amicon Concentrator (Millipore), flash-frozen, and stored at −80°C.

Lipid vesicle preparation

Three sets of lipid vesicles were prepared for HDX-MS and kinase assays: PI3P vesicles containing 45% egg yolk PC (840051C; Avanti), 20% synthetic PI3P (850150; Avanti), 25% egg yolk PE (P6386; Sigma-Aldrich), 10% porcine brain PS (840032C; Avanti); PI vesicles containing 45% egg yolk PC, 20% liver PI (840042C; Avanti), 25% egg yolk PE, 10% porcine brain PS; and PS vesicles containing 45% egg yolk PC, 25% egg yolk PE, 30% porcine brain PS. To generate vesicles, the lipid mixtures were combined in organic solvent. The mixture was then evaporated using a stream of argon gas followed by desiccation under vacuum for 45 min. The lipids were resuspended in a lipid buffer (25 mM HEPES, pH 7, 100 mM NaCl, 5% glycerol [vol/vol]), and the solution was subjected to sonication for 15 min. The vesicles were subjected to ten freeze–thaw cycles and extruded 21 times through a 100-nm filter (T and T Scientific: TT-002–0010). The extruded vesicles were aliquoted and stored at −80°C.

Kinase assays

All kinase assays were done using Transcreener ADP2 Fluorescence Intensity (FI) assays (BellBrook Labs), which measure ADP production. PI3P vesicles, PI vesicles, and PS vesicles at a final concentration of 0.2 mg/ml, ATP at a final concentration of 100 μM, and the PIKfyve core construct at final concentrations ranging from 4.12 nM to 1.0 mM were used. The protein was diluted with 5x kinase buffer (100 mM HEPES, pH 7.5, 500 mM NaCl, 0.15% CHAPS, 5 mM EGTA, 15 mM $MgCl_2$), and lipids were diluted with lipid buffer (25 mM HEPES, pH 7, 100 mM NaCl, 5% glycerol [vol/vol]).

2 μl of 2X substrate solution containing vesicles was mixed with 2 μl of 2X kinase solution, and the reaction was allowed to proceed for 60 min. The reactions were stopped with 4 μl of 2X Stop and Detect solution containing Stop and Detect buffer, 8 nM ADP Alexa Fluor 594 Tracer, and 93.7 mg/ml ADP2 Antibody-IRDye QC-1, and incubated for 50 min. The FI was measured using a SpectraMax M5 plate reader at 590 nm and emission at 620 nm. The % ATP turnover was interpolated from a standard curve (0.1–100 μM ADP) using GraphPad Prism according to the Transcreener ADP FI protocol. Only values within the dynamic range of the assay (from 0.1 to 0.5) were converted into specific activity by interpolation of the standard curve.

HDX-MS

HDX-MS sample preparation

HDX reactions comparing the PIKfyve^{CC} with and without PI3P vesicles were carried out in a 30 μl reaction volume containing 15 pmol of protein. The exchange reactions were initiated by the addition of 25 μl of D_2O buffer (20 mM imidazole, pH 7, 150 mM NaCl, 93.9% D_2O [Vol/Vol]) to 1.0 μl of protein and 4.0 μl of membrane or buffer (final D_2O concentration of 77.8%). Reactions proceeded for 3, 30, 300, and 3,000 s at room temperature before being quenched with ice-cold acidic quench buffer, resulting in a final concentration of 0.6 M guanidine HCl and 0.9% formic acid after quench. All conditions and time points were created and run in independent triplicate. Samples were flash-frozen immediately after quenching and stored at −80°C until injected into the ultra-performance liquid chromatography (UPLC) system for proteolytic cleavage, peptide separation, and injection onto a QTOF for mass analysis, as described below.

Protein digestion and MS/MS data collection

Protein samples were rapidly thawed and injected into an integrated fluidics system containing a HDx-3 PAL liquid handling robot and climate-controlled (2°C) chromatography system (LEAP Technologies), a Dionex Ultimate 3000 UHPLC system, and an Impact HD QTOF Mass spectrometer (Bruker). The full details of the automated LC system are described in Stariha et al. (2021). Samples comparing the PIKfyve^{CC} with and without PI3P vesicles, as well as samples containing the PIKfyve^{CC} with inhibitors, were run over two immobilized pepsin columns (Waters; Enzymate Protein Pepsin Column, 300 Å, 5 μm, 2.1 × 30 mm) at 350 μl/min for 3 min at 2°C. The resulting peptides were collected and desalted on a C18 trap column (ACQUITY UPLC BEH C18 1.7 mm column [2.1 × 5 mm]; 186003975; Waters). The trap was subsequently eluted in line with an ACQUITY 1.7 μm particle, 100 × 1 mm^2 C18 UPLC column (Waters), using a gradient of 3–35% B (Buffer A 0.1% formic acid; Buffer B 100% acetonitrile) over 11 min immediately followed by a gradient of 35–80% over 5 min. MS experiments were acquired over a mass range from 150 to 2,200 m/z using an electrospray ionization source operated at a temperature of 200°C and a spray voltage of 4.5 kV.

Peptide identification

Peptides were identified from the non-deuterated samples of the PIKfyve^{CC} using data-dependent acquisition following tandem MS/MS experiments (0.5-s precursor scan from 150 to 2,000 m/z; twelve 0.25-s fragment scans from 150 to 2,000 m/z). For HDX reactions comparing either the PIKfyve^{CC} apo with and without vesicles, and with and without inhibitors, the MS/MS datasets were analyzed using FragPipe v18.0 and peptide identification was carried out using a false discovery–based approach using a database of purified proteins and known contaminants (Dobbs et al., 2020). MSFragger was utilized, and the precursor mass tolerance error was set to −20 to 20 ppm. The fragment mass tolerance was set at 20 ppm. Protein digestion was set as

nonspecific, searching between lengths of 4 and 50 aa, with a mass range of 400–5,000 Da.

Mass analysis of peptide centroids and measurement of deuterium incorporation

HDExaminer software (Sierra Analytics) was used to automatically calculate the level of deuterium incorporation into each peptide. All peptides were manually inspected for correct charge state, correct retention time, appropriate selection of isotopic distribution, etc. Deuteration levels were calculated using the centroid of the experimental isotope clusters. Results are presented as relative levels of deuterium incorporation, and the only control for back exchange was the level of deuterium present in the buffer (77.8%). Differences in exchange in a peptide were considered significant if they met all three of the following criteria: ≥5% change in exchange, ≥0.45 Da difference in exchange, and a P value <0.01 using a two-tailed Student *t* test. The raw HDX data are shown in two different formats. The raw peptide deuterium incorporation graphs for a selection of peptides with significant differences are shown in Fig. 2 C, with the raw data for all analyzed peptides in the source data. To visualize differences across all peptides, we used the number of deuteron difference (#D) plots (Fig. 3 C). These plots show the total difference in deuterium incorporation over the entire H/D exchange time course, with each point indicating a single peptide. Samples were only compared within a single experiment and were never compared with experiments completed at a different time with a different final D_2O level. The data analysis statistics for all HDX-MS experiments are in Data S1 (7th Tab) according to the guidelines of Masson et al. (2019). The MS proteomics data have been deposited to the ProteomeXchange Consortium via the PRoteomic IDEntification Database partner repository (Perez-Riverol et al., 2022) with the dataset identifier PXD044706.

Online supplemental material

Fig. S1 shows validation of AlphaFold modeling of the PIKfyve complex. Fig. S2 shows detection of $PI(3,5)P_2$ using *Dd*SNXA^{PX} domain variants. Fig. S3 shows simultaneous monitoring of PI3P and $PI(3,5)P_2$ during recruitment of the PIKfyve^{CC} fragment to Rab5 endosomes. Fig. S4 shows co-localization analysis between NES$^{(2x)}$-mNG^{HO}-(2x)*Dd*SNXA^{PX} and the different endosomal markers in HEK293-AT1 cells. Fig. S5 shows assessment of the EGFP-tagged (2x) ML1N as a $PI(3,5)P_2$ reporter. Video 1 shows reappearance of PI3P-positive vesicles after apilimod treatment in HEK293A cells co-expressing the EGFP-(2x)FYVE^{Hrs} and the mRFP-FKBP-PIKfyve^{CC} enzyme. Video 2 shows disappearance of PI3P from vesicles after recruitment of the mRFP-FKBP-PIKfyve^{CC} enzyme to Rab5-positive endosomes. Video 3 shows monitoring $PI(3,5)P_2$ production using the high-avidity NES$^{(2x)}$-mNG^{HO}-(2x)*Dd*SNXA^{PX} probe upon recruitment of the PIKfyve^{CC} enzyme to Rab5-positive endosomes. Video 4 shows simultaneous monitoring of PI3P and $PI(3,5)P_2$ during recruitment of the PIKfyve^{CC} to Rab5-positive endosomes. Video 5 shows co-recruitment of Fig4 and Vac14 with the recruitable full-length FKBP-PIKfyve enzyme to mitochondria. Video 6 shows lack of co-recruitment of Fig4 and Vac14 with the recruitable FKBP-PIKfyve^{CC} fragment to mitochondria. Data S1 shows source data including HDX statistics. Table S1 lists the primers used in this study.

Data availability

The data are available from the corresponding authors upon reasonable request.

Acknowledgments

J. Burke is supported by the Natural Science and Engineering Research Council of Canada (NSERC) Discovery Grant (2020-0424) and a Michael Smith Foundation for Health Research Scholar Award (17686). I. Barlow-Busch was supported by an NSERC CGS-M scholarship. This work was partly funded by the Intramural Research Program of the *Eunice Kennedy Shriver* National Institute of Child Health and Human Development (NICHD) of the National Institutes of Health (NIH), Bethesda, MD, USA (HHS | NIH | NICHD—Z01:HD000196-25). Additional support to J.G. Pemberton was provided by a Visiting Fellowship from the NICHD, an NSERC Banting Postdoctoral Fellowship, and an NSERC Discovery Grant (2024-06589). Confocal imaging was performed at the Microscopy & Imaging Core (MIC) of the NICHD, with the kind assistance of Drs. Vincent Schram and Ling Yi.

Author contributions: J.G. Pemberton: conceptualization, data curation, formal analysis, investigation, methodology, resources, visualization, and writing—original draft, review, and editing. I. Barlow-Busch: formal analysis, investigation, resources, visualization, and writing—original draft, review, and editing. M.L. Jenkins: data curation and formal analysis. M.A.H. Parson: investigation. F. Sarnyai: formal analysis, investigation, methodology, visualization, and writing—review and editing. S.N. Bektas: data curation and formal analysis. Y.J. Kim: resources. J.E. Heuser: investigation and resources. J.E. Burke: conceptualization, formal analysis, funding acquisition, investigation, methodology, project administration, supervision, validation, visualization, and writing—original draft, review, and editing. T. Balla: conceptualization, data curation, funding acquisition, investigation, methodology, project administration, resources, supervision, validation, visualization, and writing—original draft.

Disclosures: All authors have completed and submitted the ICMJE Form for Disclosure of Potential Conflicts of Interest. J. Burke reported personal fees from Scorpion Therapeutics, other from Calico Life Sciences, personal fees from Reactive Therapeutics, and personal fees from Olema Oncology outside the submitted work. No other disclosures were reported.

Submitted: 22 August 2024
Revised: 9 January 2025
Accepted: 26 February 2025

References

Abramson, J., J. Adler, J. Dunger, R. Evans, T. Green, A. Pritzel, O. Ronneberger, L. Willmore, A.J. Ballard, J. Bambrick, et al. 2024. Accurate structure prediction of biomolecular interactions with AlphaFold 3. *Nature*. 630:493–500. https://doi.org/10.1038/s41586-024-07487-w

Baba, T., D.J. Toth, N. Sengupta, Y.J. Kim, and T. Balla. 2019. Phosphatidylinositol 4,5-bisphosphate controls Rab7 and PLEKHM1 membrane cycling during autophagosome-lysosome fusion. *EMBO J.* 38:e100312. https://doi.org/10.15252/embj.2018100312

Banerjee, S., K. Clapp, M. Tarsio, and P.M. Kane. 2019. Interaction of the late endo-lysosomal lipid PI(3,5)P2 with the Vph1 isoform of yeast V-ATPase increases its activity and cellular stress tolerance. *J. Biol. Chem.* 294: 9161–9171. https://doi.org/10.1074/jbc.RA119.008552

Baranov, M.V., F. Bianchi, A. Schirmacher, M.A.C. van Aart, S. Maassen, E.M. Muntjewerff, I. Dingjan, M. Ter Beest, M. Verdoes, S.G.L. Keyser, et al. 2019. The phosphoinositide kinase PIKfyve promotes cathepsin-S-mediated major histocompatibility complex class II antigen presentation. *iScience.* 11:160–177. https://doi.org/10.1016/j.isci.2018.12.015

Baranov, M.V., F. Bianchi, and G. van den Bogaart. 2020. The PIKfyve inhibitor apilimod: A double-edged sword against COVID-19. *Cells.* 10:30. https://doi.org/10.3390/cells10010030

Bridges, D., J.T. Ma, S. Park, K. Inoki, L.S. Weisman, and A.R. Saltiel. 2012. PI(3,5)P2 plays a role in the activation and subcellular localization of mTORC1. *Mol. Biol. Cell.* 23:2955–2962. https://doi.org/10.1091/mbc.E11-12-1034

Burke, J.E., J. Triscott, B.M. Emerling, and G.R.V. Hammond. 2023. Beyond PI3Ks: Targeting phosphoinositide kinases in disease. *Nat. Rev. Drug Discov.* 22:357–386. https://doi.org/10.1038/s41573-022-00582-5

Cai, X., Y. Xu, A.K. Cheung, R.C. Tomlinson, A. Alcázar-Román, L. Murphy, A. Billich, B. Zhang, Y. Feng, M. Klumpp, et al. 2013. PIKfyve, a class III PI kinase, is the target of the small molecular IL-12/IL-23 inhibitor apilimod and a player in Toll-like receptor signaling. *Chem. Biol.* 20:912–921. https://doi.org/10.1016/j.chembiol.2013.05.010

Choi, J., J. Chen, S.L. Schreiber, and J. Clardy. 1996. Structure of the FKBP12-rapamycin complex interacting with the binding domain of human FRAP. *Science.* 273:239–242. https://doi.org/10.1126/science.273.5272.239

Chow, C.Y., Y. Zhang, J.J. Dowling, N. Jin, M. Adamska, K. Shiga, K. Szigeti, M.E. Shy, J. Li, X. Zhang, et al. 2007. Mutation of FIG4 causes neurodegeneration in the pale tremor mouse and patients with CMT4J. *Nature.* 448:68–72. https://doi.org/10.1038/nature05876

Csordás, G., P. Várnai, T. Golenár, S. Roy, G. Purkins, T.G. Schneider, T. Balla, and G. Hajnóczky. 2010. Imaging interorganelle contacts and local calcium dynamics at the ER-mitochondrial interface. *Mol. Cell.* 39: 121–132. https://doi.org/10.1016/j.molcel.2010.06.029

Dobbs, J.M., M.L. Jenkins, and J.E. Burke. 2020. Escherichia coli and Sf9 contaminant databases to increase efficiency of tandem mass spectrometry peptide identification in structural mass spectrometry experiments. *J. Am. Soc. Mass Spectrom.* 31:2202–2209. https://doi.org/10.1021/jasms.0c00283

Dong, X.P., D. Shen, X. Wang, T. Dawson, X. Li, Q. Zhang, X. Cheng, Y. Zhang, L.S. Weisman, M. Delling, and H. Xu. 2010. PI(3,5)P(2) controls membrane trafficking by direct activation of mucolipin Ca(2+) release channels in the endolysosome. *Nat. Commun.* 1:38. https://doi.org/10.1038/ncomms1037

Dove, S.K., F.T. Cooke, M.R. Douglas, L.G. Sayers, P.J. Parker, and R.H. Michell. 1997. Osmotic stress activates phosphatidylinositol-3,5-bisphosphate synthesis. *Nature.* 390:187–192. https://doi.org/10.1038/36613

Dove, S.K., K. Dong, T. Kobayashi, F.K. Williams, and R.H. Michell. 2009. Phosphatidylinositol 3,5-bisphosphate and Fab1p/PIKfyve underPPIn endo-lysosome function. *Biochem. J.* 419:1–13. https://doi.org/10.1042/BJ20081950

Duex, J.E., F. Tang, and L.S. Weisman. 2006. The Vac14p-Fig4p complex acts independently of Vac7p and couples PI3,5P2 synthesis and turnover. *J. Cell Biol.* 172:693–704. https://doi.org/10.1083/jcb.200512105

Filonov, G.S., K.D. Piatkevich, L.M. Ting, J. Zhang, K. Kim, and V.V. Verkhusha. 2011. Bright and stable near-infrared fluorescent protein for in vivo imaging. *Nat. Biotechnol.* 29:757–761. https://doi.org/10.1038/nbt.1918

Gayle, S., S. Landrette, N. Beeharry, C. Conrad, M. Hernandez, P. Beckett, S.M. Ferguson, T. Mandelkern, M. Zheng, T. Xu, et al. 2017. Identification of apilimod as a first-in-class PIKfyve kinase inhibitor for treatment of B-cell non-Hodgkin lymphoma. *Blood.* 129:1768–1778. https://doi.org/10.1182/blood-2016-09-736892

Gee, J.A., R.F. Frausto, D.W. Chung, C. Tangmonkongvoragul, D.J. Le, C. Wang, J. Han, and A.J. Aldave. 2015. Identification of novel PIKFYVE gene mutations associated with Fleck corneal dystrophy. *Mol. Vis.* 21: 1093–1100.

Gillooly, D.J., I.C. Morrow, M. Lindsay, R. Gould, N.J. Bryant, J.M. Gaullier, R.G. Parton, and H. Stenmark. 2000. Localization of phosphatidylinositol 3-phosphate in yeast and mammalian cells. *EMBO J.* 19:4577–4588. https://doi.org/10.1093/emboj/19.17.4577

Giridharan, S.S.P., G. Luo, P. Rivero-Rios, N. Steinfeld, H. Tronchere, A. Singla, E. Burstein, D.D. Billadeau, M.A. Sutton, and L.S. Weisman. 2022. Lipid kinases VPS34 and PIKfyve coordinate a phosphoinositide cascade to regulate retriever-mediated recycling on endosomes. *Elife.* 11: e69709. https://doi.org/10.7554/eLife.69709

Hammond, G.R., M.P. Machner, and T. Balla. 2014. A novel probe for phosphatidylinositol 4-phosphate reveals multiple pools beyond the Golgi. *J. Cell Biol.* 205:113–126. https://doi.org/10.1083/jcb.201312072

Hammond, G.R., S. Takasuga, T. Sasaki, and T. Balla. 2015. The ML1Nx2 phosphatidylinositol 3,5-bisphosphate probe shows poor selectivity in cells. *PLoS One.* 10:e0139957. https://doi.org/10.1371/journal.pone.0139957

Hammond, G.R.V., M.M.C. Ricci, C.C. Weckerly, and R.C. Wills. 2022. An update on genetically encoded lipid biosensors. *Mol. Biol. Cell.* 33:tp2. https://doi.org/10.1091/mbc.E21-07-0363

Hong, N.H., A. Qi, and A.M. Weaver. 2015. PI(3,5)P2 controls endosomal branched actin dynamics by regulating cortactin-actin interactions. *J. Cell Biol.* 210:753–769. https://doi.org/10.1083/jcb.201412127

Hu, J., Q. Yuan, X. Kang, Y. Qin, L. Li, Y. Ha, and D. Wu. 2015. Resolution of structure of PIP5K1A reveals molecular mechanism for its regulation by dimerization and dishevelled. *Nat. Commun.* 6:8205. https://doi.org/10.1038/ncomms9205

Hung, S.T., G.R. Linares, W.H. Chang, Y. Eoh, G. Krishnan, S. Mendonca, S. Hong, Y. Shi, M. Santana, C. Kueth, et al. 2023. PIKFYVE inhibition mitigates disease in models of diverse forms of ALS. *Cell.* 186: 786–802.e28. https://doi.org/10.1016/j.cell.2023.01.005

Hunyady, L., A.J. Baukal, Z. Gaborik, J.A. Olivares-Reyes, M. Bor, M. Szaszak, R. Lodge, K.J. Catt, and T. Balla. 2002. Differential PI 3-kinase dependence of early and late phases of recycling of the internalized AT1 angiotensin receptor. *J. Cell Biol.* 157:1211–1222. https://doi.org/10.1083/jcb.200111013

Ikonomov, O.C., D. Sbrissa, K. Delvecchio, Y. Xie, J.P. Jin, D. Rappolee, and A. Shisheva. 2011. The phosphoinositide kinase PIKfyve is vital in early embryonic development: Preimplantation lethality of PIKfyve−/− embryos but normality of PIKfyve+/− mice. *J. Biol. Chem.* 286:13404–13413. https://doi.org/10.1074/jbc.M111.222364

Jefferies, H.B., F.T. Cooke, P. Jat, C. Boucheron, T. Koizumi, M. Hayakawa, H. Kaizawa, T. Ohishi, P. Workman, M.D. Waterfield, and P.J. Parker. 2008. A selective PIKfyve inhibitor blocks PtdIns(3,5)P(2) production and disrupts endomembrane transport and retroviral budding. *EMBO Rep.* 9:164–170. https://doi.org/10.1038/sj.embor.7401155

Jin, N., Y. Jin, and L.S. Weisman. 2017. Early protection to stress mediated by CDK-dependent PI3,5P_2 signaling from the vacuole/lysosome. *J. Cell Biol.* 216:2075–2090. https://doi.org/10.1083/jcb.201611144

Jin, N., M.J. Lang, and L.S. Weisman. 2016. Phosphatidylinositol 3,5-bisphosphate: Regulation of cellular events in space and time. *Biochem. Soc. Trans.* 44:177–184. https://doi.org/10.1042/BST20150174

Jović, M., M.J. Kean, A. Dubankova, E. Boura, A.C. Gingras, J.A. Brill, and T. Balla. 2014. Endosomal sorting of VAMP3 is regulated by PI4K2A. *J. Cell Sci.* 127:3745–3756. https://doi.org/10.1242/jcs.148809

Jovic, M., M.J. Kean, Z. Szentpetery, G. Polevoy, A.C. Gingras, J.A. Brill, and T. Balla. 2012. Two PI 4-kinases control lysosomal delivery of the Gaucher disease enzyme, beta-glucocerebrosidaae. *Mol. Biol. Cell.* 23:1533–1545. https://doi.org/10.1091/mbc.E11-06-0553

Kang, Y.L., Y.Y. Chou, P.W. Rothlauf, Z. Liu, T.K. Soh, D. Cureton, J.B. Case, R.E. Chen, M.S. Diamond, S.P.J. Whelan, and T. Kirchhausen. 2020. Inhibition of PIKfyve kinase prevents infection by Zaire ebolavirus and SARS-CoV-2. *Proc. Natl. Acad. Sci. USA.* 117:20803–20813. https://doi.org/10.1073/pnas.2007837117

Kim, Y.J., N. Sengupta, M. Sohn, A. Mandal, J.G. Pemberton, U. Choi, and T. Balla. 2022. Metabolic routing maintains the unique fatty acid composition of phosphoinositides. *EMBO Rep.* 23:e54532. https://doi.org/10.15252/embr.202154532

Krausz, S., M.J. Boumans, D.M. Gerlag, J. Lufkin, A.W. van Kuijk, A. Bakker, M. de Boer, B.M. Lodde, K.A. Reedquist, E.W. Jacobson, et al. 2012. Brief report: A phase IIa, randomized, double-blind, placebo-controlled trial of apilimod mesylate, an interleukin-12/interleukin-23 inhibitor, in patients with rheumatoid arthritis. *Arthritis Rheum.* 64:1750–1755. https://doi.org/10.1002/art.34339

Lang, M.J., B.S. Strunk, N. Azad, J.L. Petersen, and L.S. Weisman. 2017. An intramolecular interaction within the lipid kinase Fab1 regulates cellular phosphatidylinositol 3,5-bisphosphate lipid levels. *Mol. Biol. Cell.* 28:858–864. https://doi.org/10.1091/mbc.e16-06-0390

Lees, J.A., P. Li, N. Kumar, L.S. Weisman, and K.M. Reinisch. 2020. Insights into lysosomal PI(3,5)P_2 homeostasis from a structural-biochemical

analysis of the PIKfyve lipid kinase complex. *Mol. Cell.* 80:736–743.e4. https://doi.org/10.1016/j.molcel.2020.10.003

Lenk, G.M., C.J. Ferguson, C.Y. Chow, N. Jin, J.M. Jones, A.E. Grant, S.N. Zolov, J.J. Winters, R.J. Giger, J.J. Dowling, et al. 2011. Pathogenic mechanism of the FIG4 mutation responsible for Charcot-Marie-Tooth disease CMT4J. *PLoS Genet.* 7:e1002104. https://doi.org/10.1371/journal.pgen.1002104

Leray, X., J.K. Hilton, K. Nwangwu, A. Becerril, V. Mikusevic, G. Fitzgerald, A. Amin, M.R. Weston, and J.A. Mindell. 2022. Tonic inhibition of the chloride/proton antiporter ClC-7 by PI(3,5)P2 is crucial for lysosomal pH maintenance. *Elife.* 11:e74136. https://doi.org/10.7554/eLife.74136

Li, S.C., T.T. Diakov, T. Xu, M. Tarsio, W. Zhu, S. Couoh-Cardel, L.S. Weisman, and P.M. Kane. 2014. The signaling lipid PI(3,5)P_2 stabilizes V_1-V(o) sector interactions and activates the V-ATPase. *Mol. Biol. Cell.* 25: 1251–1262. https://doi.org/10.1091/mbc.e13-10-0563

Li, X., X. Wang, X. Zhang, M. Zhao, W.L. Tsang, Y. Zhang, R.G. Yau, L.S. Weisman, and H. Xu. 2013. Genetically encoded fluorescent probe to visualize intracellular phosphatidylinositol 3,5-bisphosphate localization and dynamics. *Proc. Natl. Acad. Sci. USA.* 110:21165–21170. https://doi.org/10.1073/pnas.1311864110

Liang, R., J. Ren, Y. Zhang, and W. Feng. 2019. Structural conservation of the two phosphoinositide-binding sites in WIPI proteins. *J. Mol. Biol.* 431: 1494–1505. https://doi.org/10.1016/j.jmb.2019.02.019

Liu, Z., O. Chen, J.B.J. Wall, M. Zheng, Y. Zhou, L. Wang, H.R. Vaseghi, L. Qian, and J. Liu. 2017. Systematic comparison of 2A peptides for cloning multi-genes in a polycistronic vector. *Sci. Rep.* 7:2193. https://doi.org/10.1038/s41598-017-02460-2

Maib, H., P. Adarska, R. Hunton, J.H. Vines, D. Strutt, F. Bottanelli, and D.H. Murray. 2024. Recombinant biosensors for multiplex and super-resolution imaging of phosphoinositides. *J. Cell Biol.* 223:e202310095. https://doi.org/10.1083/jcb.202310095

Masson, G.R., J.E. Burke, N.G. Ahn, G.S. Anand, C. Borchers, S. Brier, G.M. Bou-Assaf, J.R. Engen, S.W. Englander, J. Faber, et al. 2019. Recommendations for performing, interpreting and reporting hydrogen deuterium exchange mass spectrometry (HDX-MS) experiments. *Nat. Methods.* 16:595–602. https://doi.org/10.1038/s41592-019-0459-y

Masson, G.R., M.L. Jenkins, and J.E. Burke. 2017. An overview of hydrogen deuterium exchange mass spectrometry (HDX-MS) in drug discovery. *Expert Opin. Drug Discov.* 12:981–994. https://doi.org/10.1080/17460441.2017.1363734

Meijer, H.J.G., N. Divecha, H. van den Ende, A. Musgrave, and T. Munnik. 1999. Hyperosmotic stress induces rapid synthesis of phosphatidyl-D-inositol 3,5-bisphosphate in plant cells. *Planta.* 208:294–298. https://doi.org/10.1007/s004250050561

Nicot, A.S., H. Fares, B. Payrastre, A.D. Chisholm, M. Labouesse, and J. Laporte. 2006. The phosphoinositide kinase PIKfyve/Fab1p regulates terminal lysosome maturation in Caenorhabditis elegans. *Mol. Biol. Cell.* 17:3062–3074. https://doi.org/10.1091/mbc.e05-12-1120

Pemberton, J.G., Y.J. Kim, J. Humpolickova, A. Eisenreichova, N. Sengupta, D.J. Toth, E. Boura, and T. Balla. 2020. Defining the subcellular distribution and metabolic channeling of phosphatidylinositol. *J. Cell Biol.* 219: e201906130. https://doi.org/10.1083/jcb.201906130

Perez-Riverol, Y., J. Bai, C. Bandla, D. García-Seisdedos, S. Hewapathirana, S. Kamatchinathan, D.J. Kundu, A. Prakash, A. Frericks-Zipper, M. Eisenacher, et al. 2022. The PRIDE database resources in 2022: A hub for mass spectrometry-based proteomics evidences. *Nucleic Acids Res.* 50: D543–D552. https://doi.org/10.1093/nar/gkab1038

Qiao, Y., J.E. Choi, J.C. Tien, S.A. Simko, T. Rajendiran, J.N. Vo, A.D. Delekta, L. Wang, L. Xiao, N.B. Hodge, et al. 2021. Autophagy inhibition by targeting PIKfyve potentiates response to immune checkpoint blockade in prostate cancer. *Nat. Cancer.* 2:978–993. https://doi.org/10.1038/s43018-021-00237-1

Rao, V.D., S. Misra, I.V. Boronenkov, R.A. Anderson, and J.H. Hurley. 1998. Structure of type IIbeta phosphatidylinositol phosphate kinase: A protein kinase fold flattened for interfacial phosphorylation. *Cell.* 94: 829–839. https://doi.org/10.1016/S0092-8674(00)81741-9

Rivero-Ríos, P., and L.S. Weisman. 2022. Roles of PIKfyve in multiple cellular pathways. *Curr. Opin. Cell Biol.* 76:102086. https://doi.org/10.1016/j.ceb.2022.102086

Robinson, M.S., D.A. Sahlender, and S.D. Foster. 2010. Rapid inactivation of proteins by rapamycin-induced rerouting to mitochondria. *Dev. Cell.* 18: 324–331. https://doi.org/10.1016/j.devcel.2009.12.015

Rudge, S.A., D.M. Anderson, and S.D. Emr. 2004. Vacuole size control: Regulation of PtdIns(3,5)P2 levels by the vacuole-associated Vac14-Fig4 complex, a PtdIns(3,5)P2-specific phosphatase. *Mol. Biol. Cell.* 15: 24–36. https://doi.org/10.1091/mbc.e03-05-0297

Rusten, T.E., L.M. Rodahl, K. Pattni, C. Englund, C. Samakovlis, S. Dove, A. Brech, and H. Stenmark. 2006. Fab1 phosphatidylinositol 3-phosphate 5-kinase controls trafficking but not silencing of endocytosed receptors. *Mol. Biol. Cell.* 17:3989–4001. https://doi.org/10.1091/mbc.e06-03-0239

Sands, B.E., E.W. Jacobson, T. Sylwestrowicz, Z. Younes, G. Dryden, R. Fedorak, and S. Greenbloom. 2010. Randomized, double-blind, placebo-controlled trial of the oral interleukin-12/23 inhibitor apilimod mesylate for treatment of active Crohn's disease. *Inflamm. Bowel Dis.* 16: 1209–1218. https://doi.org/10.1002/ibd.21159

Sbrissa, D., O.C. Ikonomov, H. Fenner, and A. Shisheva. 2008. ArPIKfyve homomeric and heteromeric interactions scaffold PIKfyve and Sac3 in a complex to promote PIKfyve activity and functionality. *J. Mol. Biol.* 384: 766–779. https://doi.org/10.1016/j.jmb.2008.10.009

Sbrissa, D., O.C. Ikonomov, and A. Shisheva. 2002. Phosphatidylinositol 3-phosphate-interacting domains in PIKfyve. Binding specificity and role in PIKfyve. Endomenbrane localization. *J. Biol. Chem.* 277:6073–6079. https://doi.org/10.1074/jbc.M110194200

Schindelin, J., I. Arganda-Carreras, E. Frise, V. Kaynig, M. Longair, T. Pietzsch, S. Preibisch, C. Rueden, S. Saalfeld, B. Schmid, et al. 2012. Fiji: An open-source platform for biological-image analysis. *Nat. Methods.* 9: 676–682. https://doi.org/10.1038/nmeth.2019

Sharma, G., C.M. Guardia, A. Roy, A. Vassilev, A. Saric, L.N. Griner, J. Marugan, M. Ferrer, J.S. Bonifacino, and M.L. DePamphilis. 2019. A family of PIKFYVE inhibitors with therapeutic potential against autophagy-dependent cancer cells disrupt multiple events in lysosome homeostasis. *Autophagy.* 15:1694–1718. https://doi.org/10.1080/15548627.2019.1586257

Shisheva, A. 2012. PIKfyve and its Lipid products in health and in sickness. *Curr. Top. Microbiol. Immunol.* 362:127–162. https://doi.org/10.1007/978-94-007-5025-8_7

Stariha, J.T.B., R.M. Hoffmann, D.J. Hamelin, and J.E. Burke. 2021. Probing protein-membrane interactions and dynamics using hydrogen-deuterium exchange mass spectrometry (HDX-MS). *Methods Mol. Biol.* 2263:465–485. https://doi.org/10.1007/978-1-0716-1197-5_22

Stjepanovic, G., S. Baskaran, M.G. Lin, and J.H. Hurley. 2017. Vps34 kinase domain dynamics regulate the autophagic PI 3-kinase complex. *Mol. Cell.* 67:528–534.e3. https://doi.org/10.1016/j.molcel.2017.07.003

Suh, B.C., T. Inoue, T. Meyer, and B. Hille. 2006. Rapid chemically induced changes of PtdIns(4,5)P2 gate KCNQ ion channels. *Science.* 314: 1454–1457. https://doi.org/10.1126/science.1131163

Sultana, F., L.R. Morse, G. Picotto, W. Liu, P.K. Jha, P.R. Odgren, and R.A. Battaglino. 2020. Snx10 and PIKfyve are required for lysosome formation in osteoclasts. *J. Cell. Biochem.* 121:2927–2937. https://doi.org/10.1002/jcb.29534

Sumita, K., Y.H. Lo, K. Takeuchi, M. Senda, S. Kofuji, Y. Ikeda, J. Terakawa, M. Sasaki, H. Yoshino, N. Majd, et al. 2016. The lipid kinase PI5P4Kβ is an intracellular GTP sensor for metabolism and tumorigenesis. *Mol. Cell.* 61:187–198. https://doi.org/10.1016/j.molcel.2015.12.011

Vadas, O., M.L. Jenkins, G.L. Dornan, and J.E. Burke. 2017. Using hydrogen-deuterium exchange mass spectrometry to examine protein-membrane interactions. *Methods Enzymol.* 583:143–172. https://doi.org/10.1016/bs.mie.2016.09.008

Várnai, P., and T. Balla. 2006. Live cell imaging of phosphoinositide dynamics with fluorescent protein domains. *Biochim. Biophys. Acta.* 1761:957–967. https://doi.org/10.1016/j.bbalip.2006.03.019

Varnai, P., B. Thyagarajan, T. Rohacs, and T. Balla. 2006. Rapidly inducible changes in phosphatidylinositol 4,5-bisphosphate levels influence multiple regulatory functions of the lipid in intact living cells. *J. Cell Biol.* 175:377–382. https://doi.org/10.1083/jcb.200607116

Vicinanza, M., V.I. Korolchuk, A. Ashkenazi, C. Puri, F.M. Menzies, J.H. Clarke, and D.C. Rubinsztein. 2015. PI(5)P regulates autophagosome biogenesis. *Mol. Cell.* 57:219–234. https://doi.org/10.1016/j.molcel.2014.12.007

Vines, J.H., H. Maib, C.M. Buckley, A. Gueho, Z. Zhu, T. Soldati, D.H. Murray, and J.S. King. 2023. A PI(3,5)P2 reporter reveals PIKfyve activity and dynamics on macropinosomes and phagosomes. *J. Cell Biol.* 222: e202209077. https://doi.org/10.1083/jcb.202209077

Wada, Y., I. Cardinale, A. Khatcherian, J. Chu, A.B. Kantor, A.B. Gottlieb, N. Tatsuta, E. Jacobson, J. Barsoum, and J.G. Krueger. 2012. Apilimod inhibits the production of IL-12 and IL-23 and reduces dendritic cell infiltration in psoriasis. *PLoS One.* 7:e35069. https://doi.org/10.1371/journal.pone.0035069

Wada, Y., R. Lu, D. Zhou, J. Chu, T. Przewloka, S. Zhang, L. Li, Y. Wu, J. Qin, V. Balasubramanyam, et al. 2007. Selective abrogation of Th1 response by STA-5326, a potent IL-12/IL-23 inhibitor. *Blood*. 109:1156–1164. https://doi.org/10.1182/blood-2006-04-019398

Weckerly, C.C., and G.R.V. Hammond. 2023. Molding a PI(3,5)P2 biosensor. *J. Cell Biol.* 222:e202308004. https://doi.org/10.1083/jcb.202308004

Wills, R.C., B.D. Goulden, and G.R.V. Hammond. 2018. Genetically encoded lipid biosensors. *Mol. Biol. Cell*. 29:1526–1532. https://doi.org/10.1091/mbc.E17-12-0738

Wu, J.Z., J.G. Pemberton, S. Morioka, J. Sasaki, P. Bablani, T. Sasaki, T. Balla, S. Grinstein, and S. Freeman. 2025. Sorting nexin 10 regulates lysosomal ionic homeostasis via ClC-7 by controlling PI(3,5)P_2. *J. Cell Biol.* https://doi.org/10.1083/jcb.202408174

Xu, T., Q. Gan, B. Wu, M. Yin, J. Xu, X. Shu, and J. Liu. 2020. Molecular basis for PI(3,5)P_2 recognition by SNX11, a protein involved in lysosomal degradation and endosome homeostasis regulation. *J. Mol. Biol.* 432:4750–4761. https://doi.org/10.1016/j.jmb.2020.06.010

Yamamoto, A., D.B. DeWald, I.V. Boronenkov, R.A. Anderson, S.D. Emr, and D. Koshland. 1995. Novel PI(4)P 5-kinase homologue, Fab1p, essential for normal vacuole function and morphology in yeast. *Mol. Biol. Cell*. 6:525–539. https://doi.org/10.1091/mbc.6.5.525

Yu, L., Y. Chen, and S.A. Tooze. 2018. Autophagy pathway: Cellular and molecular mechanisms. *Autophagy*. 14:207–215. https://doi.org/10.1080/15548627.2017.1378838

Zhang, Y., S.N. Zolov, C.Y. Chow, S.G. Slutsky, S.C. Richardson, R.C. Piper, B. Yang, J.J. Nau, R.J. Westrick, S.J. Morrison, et al. 2007. Loss of Vac14, a regulator of the signaling lipid phosphatidylinositol 3,5-bisphosphate, results in neurodegeneration in mice. *Proc. Natl. Acad. Sci. USA*. 104:17518–17523. https://doi.org/10.1073/pnas.0702275104

Zolov, S.N., D. Bridges, Y. Zhang, W.W. Lee, E. Riehle, R. Verma, G.M. Lenk, K. Converso-Baran, T. Weide, R.L. Albin, et al. 2012. In vivo, Pikfyve generates PI(3,5)P2, which serves as both a signaling lipid and the major precursor for PI5P. *Proc. Natl. Acad. Sci. USA*. 109:17472–17477. https://doi.org/10.1073/pnas.1203106109

JCB

Supplemental material

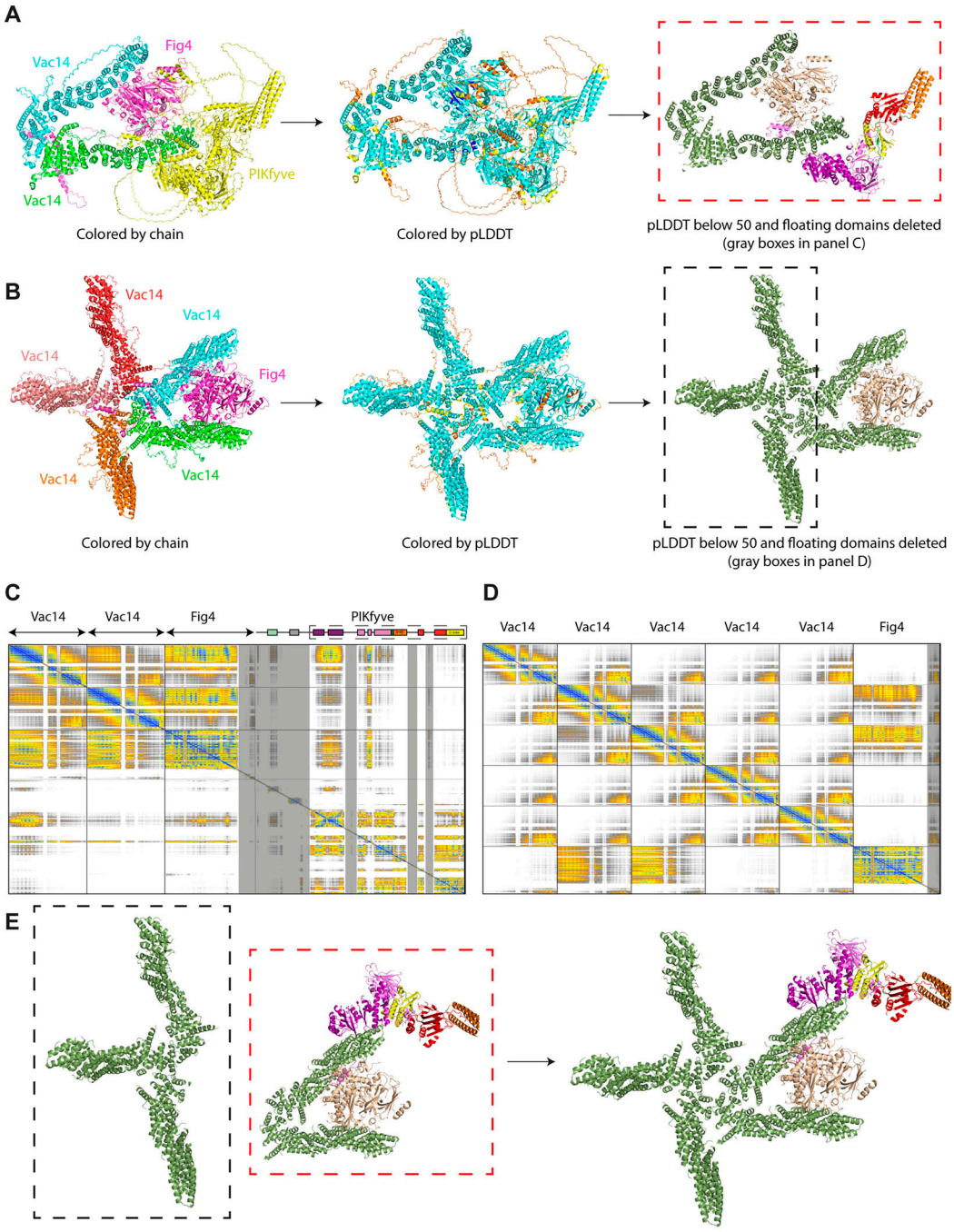

Figure S1. **Validation of AlphaFold modeling of the PIKfyve complex. (A)** Flow path for processing the AlphaFold3 search of PIKfyve with Fig4 and two copies of Vac14. The model is colored by chain to identify each protein, then colored by pLDDT to indicate regions of high and low confidence. The final panel shows the structure used in Fig. 1 A, where residues with a pLDDT score <50 and domains that do not form high-confidence contacts with the complex have been deleted. **(B)** Flow path for processing the AlphaFold3 search of Fig4 and five copies of Vac14. The model is colored by chain to identify each protein, then colored by pLDDT to indicate regions of high and low confidence. The final panel shows the structure used in Fig. 1 A, where residues with a pLDDT score <50 and domains that do not form high-confidence contacts with the complex have been deleted. **(C)** PAE for AlphaFold3 search of PIKfyve with Fig4 and two copies of Vac14. The colors indicate the PAE and are colored according to the legend. Note that the PAE plot is not an inter-residue distance map or a contact map. Instead, the red-blue color indicates the expected distance error. The color at (x, y) corresponds to the expected distance error in residue x's position (Angstroms), when the predictions are aligned on residue y (more information can be found at https://alphafold.ebi.ac.uk/). The regions highlighted in gray indicate domains that have been deleted because they do not form high-confidence interfaces with the complex. **(D)** PAE for AlphaFold3 search of Fig4 and five copies of Vac14. The colors indicate the PAE and are colored according to the legend. Note that the PAE plot is not an inter-residue distance map or a contact map. Instead, the red-blue color indicates the expected distance error. The color at (x, y) corresponds to the expected distance error in residue x's position (Angstroms), when the predictions are aligned on residue y (more information can be found at https://alphafold.ebi.ac.uk/). The regions highlighted in gray indicate domains that have been deleted because they do not form high-confidence interfaces with the complex. **(E)** Flow path for how the full model of the PIKfyve complex was generated for Fig. 1 A. The searches described in A and B were aligned at Fig4, and the two overlapping Vac14 arms were deleted from the Vac14 pentamer. PAE, predicted aligned error.

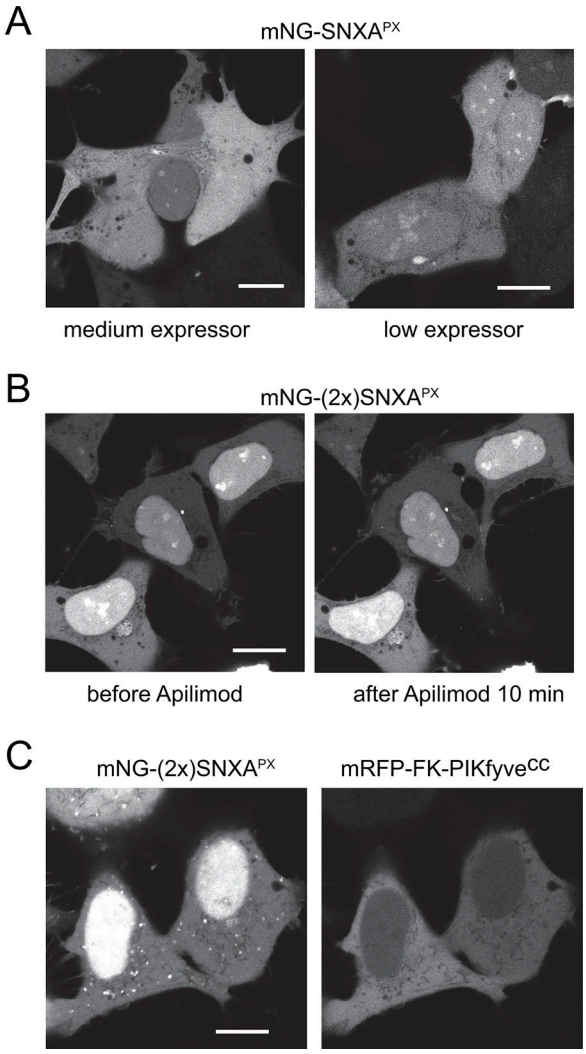

Figure S2. **Detection of PI(3,5)P_2 using *Dd*SNXA^{PX} domain variants. (A and B)** Confocal images of HEK293A cells expressing the single (A) or tandem (B) version of the *Dd*SNXA^{PX} probe fused to mNG^{HO}. In these cells, no endocytic structures were decorated with either construct regardless of how low the relative expression levels were. In most cells, a bright dot was visible at the centrosome region that did not disappear after apilimod treatment (1 μM). Similarly, the nuclear and nucleolar enrichment was also not affected by apilimod treatment. In subsequent versions of the probes, a tandem NES$^{(2x)}$ was added to prevent the prominent nuclear localization. **(C)** Co-expression of the FKBP-PIKfyve^{CC} fragment with the tandem NES$^{(2x)}$-mNG^{HO}-(2x)*Dd*SNXA^{PX} shows localization of the reporter to endocytic structures (scale bars = 10 μm).

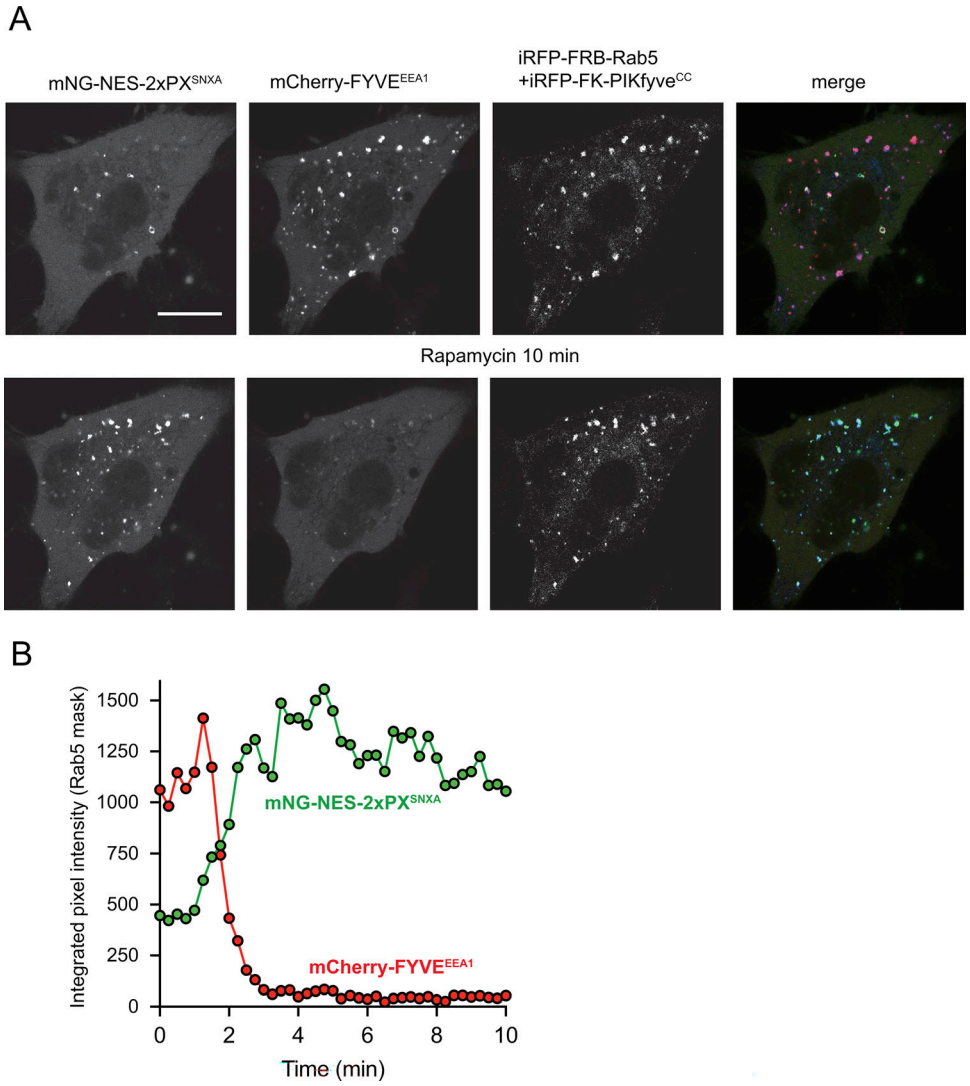

Figure S3. **Simultaneous monitoring of PI3P and PI(3,5)P_2 during recruitment of the PIKfyve^{CC} fragment to Rab5 endosomes. (A)** Confocal images of HEK293A cells expressing mCherry-FYVE^{EEA1}, NES$^{(2x)}$-mNG^{HO}-(2x)*Dd*SNXA^{PX}, iRFP-FKBP-PIKfyve^{CC}, and a Rab5-targeted FRB fragment (iRFP-FRB-Rab5). Rapamycin addition (100 nM) causes the appearance of the PI(3,5)P_2 reporter and the simultaneous disappearance of the PI3P sensor in the Rab5 compartment. **(B)** Quantification of the changes in time-lapse images for the cell shown in A. Similar results were recorded in four separate dishes in separate experiments (scale bars = 10 µm).

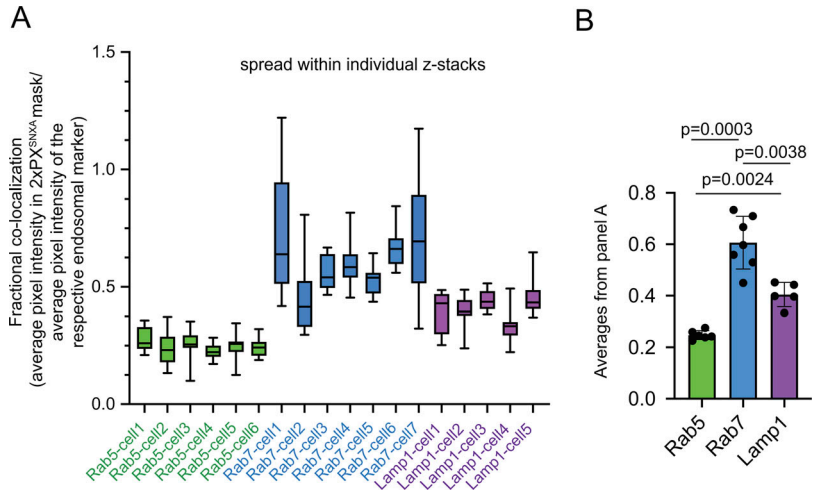

Figure S4. **Co-localization analysis between NES$^{(2x)}$-mNG^{HO}-(2x)*Dd*SNXA^{PX} and the different endosomal markers in HEK293-AT1 cells.** Cells were transfected with NES$^{(2x)}$-mNG^{HO}-(2x)*Dd*SNXA^{PX} and the mCherry-tagged indicated endosomal marker or LysoTracker Red, and z-stacks of confocal images were recorded from individual cells. A mask was then generated using the thresholded PI(3,5)P_2 image and used to calculate the average pixel intensities of the background-subtracted endosomal marker image in that mask throughout the z-planes. These values were then divided by the respective average pixel intensity values obtained for the entire thresholded endosomal marker throughout the z-planes. **(A and B)** Fractional co-localization values for the individual cells across the individual z-planes as box-and-whisker diagrams, with (B) average values analyzed using Welch's ANOVA test with multiple comparison.

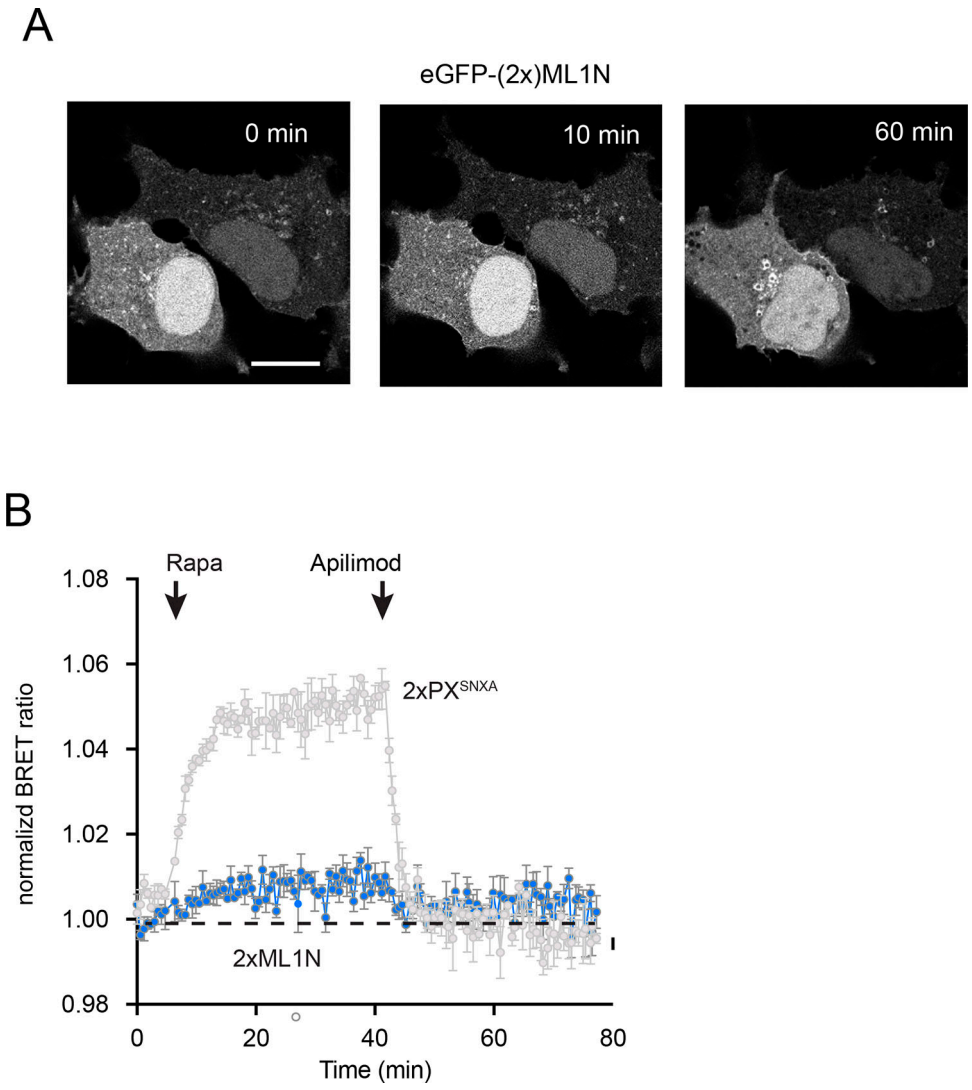

Figure S5. **Assessment of the EGFP-tagged (2x)ML1N as a PI(3,5)P_2 reporter. (A)** Expression of the EGFP-tagged (2x)ML1N reporter (Li et al., 2013) in HEK293A cells shows localization of this probe to endocytic structures, which are not eliminated even by prolonged treatment with apilimod (1 µM). **(B)** Rab5-specific BRET-based biosensor that contains the (2x)ML1N segment (sLuc-(2x)ML1N-tPT2A-mVenus-Rab5) shows a weak but clear response to acute PI(3,5)P_2 generation by FKBP-PIKfyve^{CC} recruitment. Grand averages (±SEM) are presented from three experiments, with distinct treatments performed in triplicate within each replicate. To allow for direct comparisons, we included the response of the (2x)*Dd*SNXA^{PX} BRET reporter shown in Fig. 8 D (gray symbols).

Video 1. **Reappearance of PI3P-positive vesicles after apilimod treatment in HEK293A cells co-expressing the EGFP-(2x)FYVE^{Hrs} and the mRFP-FKBP-PIKfyve^{CC} enzyme.** Note that no PI3P signal is detected in HEK293A cells expressing the FKBP-PIKfyve^{CC} enzyme (the red channel is not shown for simplicity). However, after treatment with apilimod (1 µM), PI3P-positive endosomes start to appear. This movie is played with a speed of 10 frames per second, and frames were recorded every 15 s. Apilimod (1 µM) was added after the fourth frame.

Video 2. **Disappearance of PI3P from vesicles after recruitment of the mRFP-FKBP-PIKfyve^{CC} enzyme to Rab5-positive endosomes.** HEK293A cells were transfected with the PI3P sensor, EGFP-FYVE^{EEA1}, together with the recruitable mRFP-FKBP-PIKfyve^{CC} enzyme and iRFP-FRB-Rab5. Cells that express all three constructs and still show PI3P signal in their endosomes were subjected to rapamycin treatment. This movie is played with a speed of 15 frames per second, and frames were recorded every 15 s. Rapamycin (100 nM) was added after the fourth and apilimod (1 µm) after the 45th frame.

Video 3. **Monitoring PI(3,5)P_2 production using the high-avidity NES$^{(2x)}$-mNG^{HO}-(2x)*Dd*SNXA^{PX} probe upon recruitment of the PIKfyve^{CC} enzyme to Rab5-positive endosomes.** HEK293A cells were transfected with the PI(3,5)P_2 sensor, NES$^{(2x)}$-mNG^{HO}-(2x)*Dd*SNXA^{PX}, together with the recruitable mRFP-FKBP-PIKfyve^{CC} enzyme and iRFP-FRB-Rab5. This movie is played with a speed of 6 frames per second, and frames were recorded every 30 s. Rapamycin (100 nM) was added after the fourth frame and apilimod (1 µM) at frame 20.

Video 4. **Simultaneous monitoring PI3P and PI(3,5)P_2 during recruitment of the PIKfyve^{CC} to Rab5-positive endosomes.** Confocal images of HEK293A cells expressing mCherry-FYVE^{EEA1}, NES$^{(2x)}$-mNG^{HO}-(2x)*Dd*SNXA^{PX}, iRFP-FKBP-PIKfyve^{CC}, and a Rab5-targeted FRB fragment (iRFP-FRB-Rab5). Rapamycin addition causes the appearance of the PI(3,5)P_2 reporter and the simultaneous disappearance of the PI3P sensor in the Rab5-positive compartment. Individual channels associated with the mNG (top left), mCherry (top right), their overlay (bottom left), and iRFP (bottom right) are shown. This movie is played with a speed of 15 frames per second, and frames were recorded every 15 s. Rapamycin (100 nM) was added after the fourth frame. Note that the signal from the iRFP-FKBP-PIKfyve^{CC} fragment is practically invisible against the iRFP-FRB-Rab5 signal, yet its enzymatic effect is clearly demonstrated by the changes in the localization of the lipid reporters after the addition of rapamycin.

Video 5. **Co-recruitment of Fig4 and Vac14 with the recruitable full-length FKBP-PIKfyve enzyme to mitochondria.** A recruitable version of the full-length PIKfyve enzyme (iRFP-FKBP-PIKfyve^{FL}) was co-transfected with mCherry-Vac14 and Fig4-mNG together with an OMM-targeted FRB recruiter (AKAP-FRB-ECFP). Rapamycin-induced translocation of FKBP-PIKfyve^{FL} to the mitochondria also caused translocation of Vac14 and Fig4, which is consistent with their association. Individual channels are shown as ECFP (top left), mNG (top right), mCherry (bottom left), and iRFP (bottom right). This movie is played with a speed of 15 frames per second, and frames were recorded every 15 s. Rapamycin (100 nM) was added after the fourth frame.

Video 6. **Lack of co-recruitment of Fig4 and Vac14 with the recruitable FKBP-PIKfyve^{CC} fragment to mitochondria.** A recruitable version of the PIKfyve^{CC} fragment (iRFP-FKBP-PIKfyve^{CC}) was co-transfected with mCherry-Vac14 and Fig4-mNG together with an OMM-targeted FRB recruiter (AKAP-FRB-ECFP). Rapamycin-induced translocation of the FKBP-PIKfyve^{CC} to the mitochondria failed to cause translocation of Vac14 and Fig4 to the mitochondria, suggesting that it does not interact with these two protein partners. Individual channels are shown as ECFP (top left), mNG (top right), mCherry (bottom left), and iRFP (bottom right). This movie is played with a speed of 15 frames per second, and frames were recorded every 15 s. Rapamycin (100 nM) was added after the fourth frame.

Provided online is Data S1 and Table S1. Data S1 shows source data including HDX statistics. Table S1 lists the primers used in this study.